BACHELOR

Characterising transparent contacts for InP nanowire solar cells

Op de Beeck, J.

Award date:
2015

Technische Universiteit
Eindhoven
University of Technology

Bachelor thesis in cooperation with PSN

Characterising transparent contacts for InP nanowire solar cells

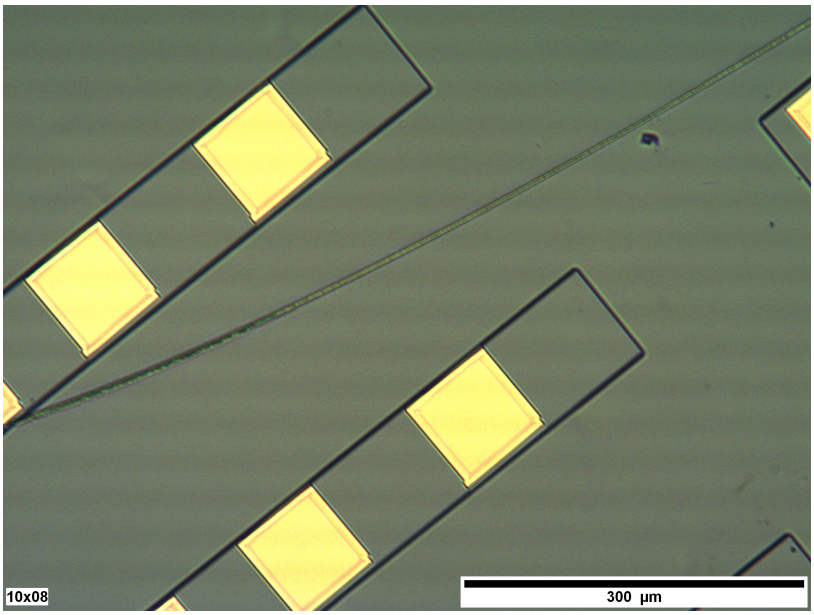

Jonathan Op de Beeck

Contents

1 Motivation for this project

Generating energy from renewable sources in order to replace fossil fuels is a topic of both social and scientific interest. As currently the majority of the energy used by humans is created by burning fossil fuels [1], which are on the one hand limited in supply [2] and on the other hand are raising serious environmental concerns, significant scientific advancements are necessary in order to replace energy from fossil fuels with efficient renewable energy. Potential renewable energy sources are windpower, hydropower, nuclear power and solar power [2]. Solar power, which is the direct conversion from sun-light to electric energy, is currently seen as the most abundant renewable energy source [3] and hence of particular scientific interest.

According to the International Energy Agency, IEA, solar photovoltaic energy , together with solar thermal energy, will be as cost efficient as fossil fuels by 2030 [3]. Progress in the development of solar cells has already led to a continuous drop in the price of solar cells over the last 30 years [4] as can be seen in figure 1. The price drop is due to intensive research resulting in cheaper and more efficient solar cells. Here we are aiming to develop new solar cells based on nanowires that may allow to continue this trend by improving the conversion efficiency of solar cells, allowing for cheaper fabrication processes, and limiting the amount of materials necessary to build the solar cell.

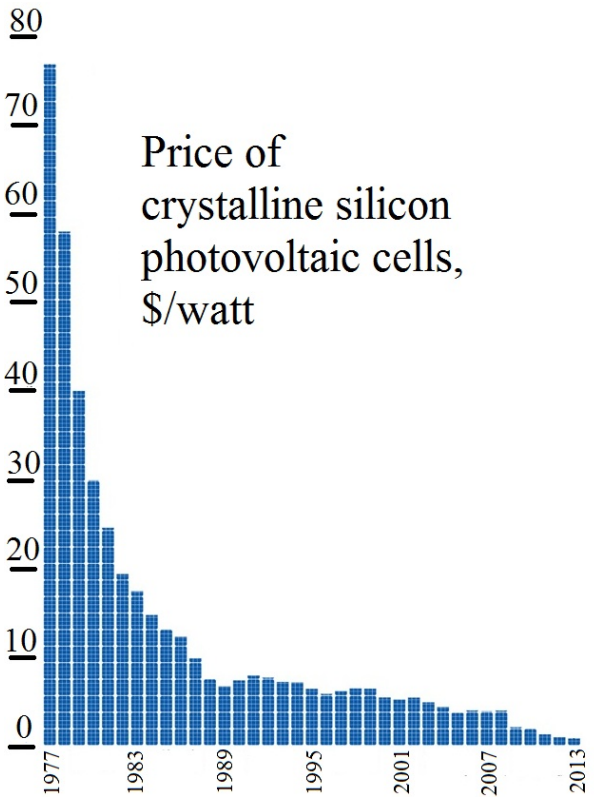

Figure 1: Prices for solar cells in the past 30 years. [4]

This thesis will consider the promising alternative of InP nanowire based solar cells. [5] InP nanowires are an alternative for the common crystalline silicon thin film solar cells. The use of InP nanowires provides many advantages over the common solar cell as elaborated in the following paragraphs. We will show the improved optical properties, band gap energy and low surface recombination rate and argue why cheaper fabrication processes are possible. Finally we will accentuate the importance of the electrical contacts in the solar cell device which will be the main subject of this thesis.

The optical properties of an array of nanowires is significantly different from thin films. The main difference lies in the fact that the absorption losses are different. Thin film solar cells typically suffer losses from reflection, the photons are immediately scattered back, and transmission, the semiconductor thin film does not have sufficient light trapping to capture all the photons.

To reduce the effect of the loss by reflection regular crystalline silicon devices are coated with several layers having a refractive index between the semiconductors and air which decreases reflection. [6] A gradual shift of the refractive index from air to semiconductor is also obtained by using tapered nanowires (often referred to as nanocones), visible on the left side of figure 2, instead of nanowires with a straight edge. The improved absorption can be observed on the right side of figure 2 .[7]

Nanowires also provide an improvement for the loss by transmission. It can be shown that nanowires can act as antennas for certain resonant wavelengths. These wavelengths bounce around in the wire which improves absorption. [8]

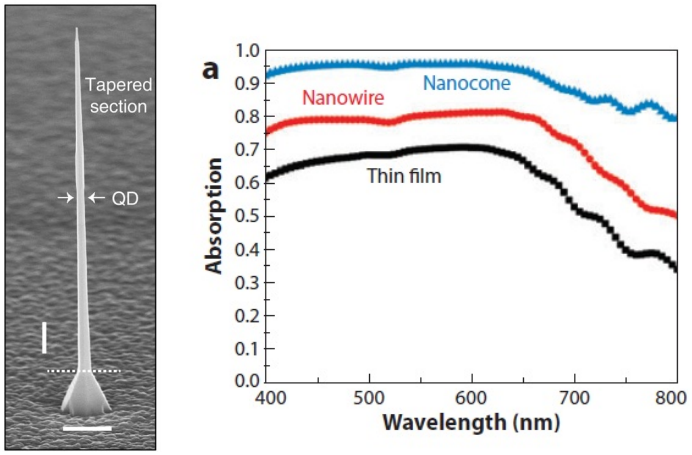

Figure 2: Left: SEM image of tapered InP nanowire containing a single InAsP quantum dot (QD).[9] Right: Absorption properties of nanowires and nanocones.[7]

Here we work with InP nanowires because of the unique properties of InP. InP is

well suited for solar cells because of its direct bandgap of 1.34 eV which is ideal for solar-cell efficiency as calculated by S.M. Sze.[10] The result of this calculation can be observed in figure 3 . For this reason others before us reported good results with the material. [11].

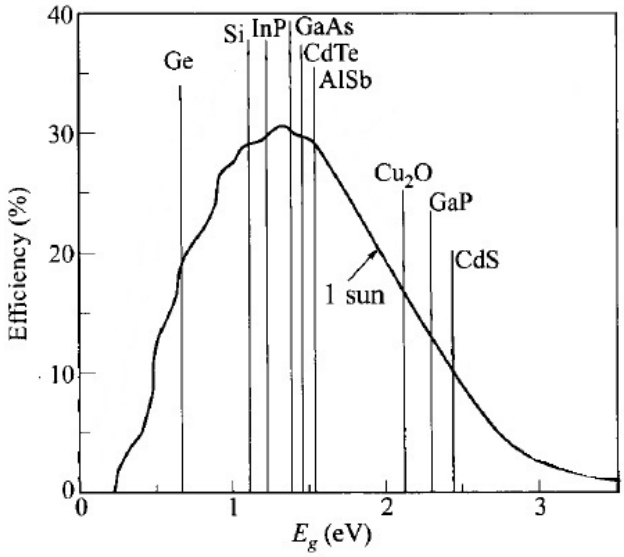

Figure 3: The value for the band gap energy E_g (eV) to achieve ideal solar-cell efficiency.This is at one sun, 300K and assumes a universal air mass coëffcient AM of 1.5 . [10]

InP has another interesting characteristic; an exceptionally low surface recombination velocity (170 cm/s) at room temperature. [12] This result enhances the potential of the material for photovoltaic applications.[6] Surface recombination can have a huge impact on the short-circuit current and the open-circuit voltage.[6] Particularly for nanowires based solar cells this plays an important role since there is a lot of surface and many charge carriers could be lost. This lowers the need of passivating the surface to reduce surface recombination, for example a thermally grown silicon dioxide or silicon nitride layer.[6]

On top of technological advantages nanowires based solar cells open doors for new, cheaper processing and fabrication steps. Nanowires relax the requirements for achieving a high efficiency because of the following reasons:

- A lower purity standard contributes to suppressing the costs.[7]
- Less material is needed compared to planar layers.
- The removed need for a lattice matching-substrate, which promotes the choice for cheap substrates and opens doors for a broader range of usable materials.[7]

The latter of these reasons is a consequence of their small cross-sectional area which permits lattice-mismatch strain to be accommodated by elastic relaxation at the nanowire surfaces instead of plastic relaxation in the form of dislocations.[13] [14]

Solar energy is the direct conversion from sun-light to electric energy. Incident photon illumination can create electron-hole pairs in the space charge region of a junction. Electrons and holes will be guided by an electrical field and extracted by contacts resulting in a photocurrent. Ohmic contacts ensure a good energy conversion efficiency. The top contact should be transparent for light to pass to the InP layer. The bottom contact is usually chosen reflective. [7] Optimising the device by using more efficient nanowires and better nano structures is critical to achieve a high efficiency. However the contacts are often neglected and not optimised albeit they are a critical part of the device.[15]

The key properties a transparent conducting oxide (TCO) top contact should have is transparency and good conductance (a low sheet resistance). While the transparency condition is normally satisfied some optimization can be achieved on the electrical part. Another important physical property is the contact between the metal TCO and the semiconductor InP. A current travelling laterally trough device must pass this interface. The magnitude of this contact resistance depends on the semiconductor and its doping level near the surface and the metal contact. It is known that a high contact resistance ($> 10^{-3}\Omega cm^2$) is a potential source of power loss for solar cell devices [15].

In this investigation the electrical properties of several types of top contacts will be considered. We will look into sheet and contact resistances and provide an answer to which top contact is more beneficial in combination with InP for the operation of the device. We will elaborate on several materials including ZnO, and AlZnO (Al doped ZnO). Different thicknesses and different levels of doping will be considered.

This thesis contains the processing, measurements and analysis of the different materials. First a description of the solar cell device will be given. Then the deposition of the TCO together with its characterisation will be discussed. Measurements will be supported by numerical simulations using the finite element method (FEM).

2 The solar cell

The components of our solar cell are the InP nanowires, a front contact and a back contact. Nanowires are grown as described by Y. Cui based on the vapor-liquid-solid mechanism. [11] In the following paragraphs we will elaborate on the construction of the full solar cell device based on these nanowires. We will start off with the processing of the substrate followed by the nano imprint lithography. Afterwards the growth and etching of the wires is considered. Finally the contacts are formed.

The substrate used for the growth of the nanowires is a Zn-doped (p-doping) (111)B InP substrate (Only P atoms terminated). This is because the growth process is well known for this structure. On the backside a heavily doped ($N_a = 1.2.10^{19} cm^{-3}$) p^+-InGaAs layer of 200 nm is grown. This ensures a P-doped back contact coupled to the p-part of the junction in the nanowires.

Nanoimprint lithography is used to form an array of gold particles used to catalyse the growth the nanowires. An array of 130 nm diameter Au particles with 500 nm spacing is prepared. An example is shown in figure 4. [16] Our nanowires are grown in an Aixtron CCS MOVPE system using trimethylindium (TMI) and phosphine (PH_3) at 450 °C using the vapor-liquid-solid growth mechanism with the gold particles as a catalyst. Dopants are inserted in the nanowires during the growth. Diethylzinc and H_2S are used to introduce zinc and sulphur as respectively p-type and n-type dopants. The grown nanowires can be observed in figure 5.

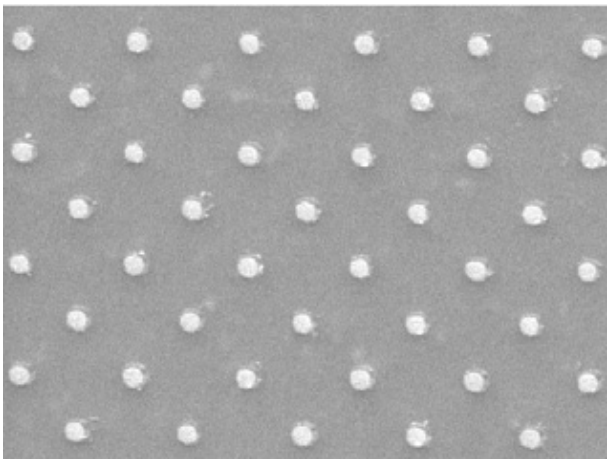

Figure 4: SEM images of an array of gold particles. [16]

During the growth in situ etching with HCl is applied. A $2.83.10^{-5}$ molar fraction is introduced to reduce the radial growth. This etching improves the uniformity of the nanowires and improves the electrical properties. However it reduces the tapering and therefore the absorption as discussed earlier. Albeit this is true in

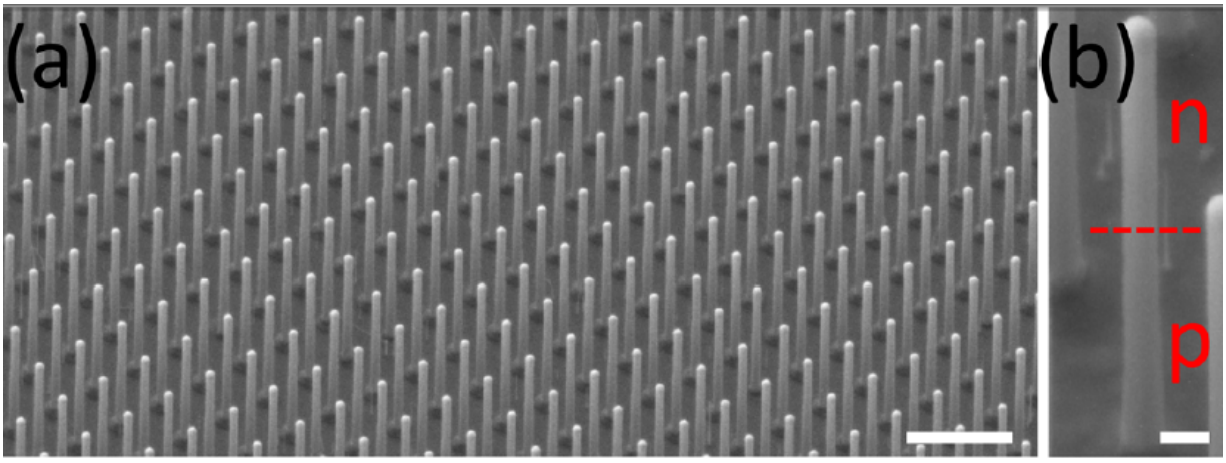

Figure 5: (a)SEM images of the grown nanowires. (b) SEM image of the PN junction. [11]

situ etching is still profitable mainly because of the decrease of shunts which form radially between the wires. The result of in situ etching for different molar fractions can be seen in figure 6.

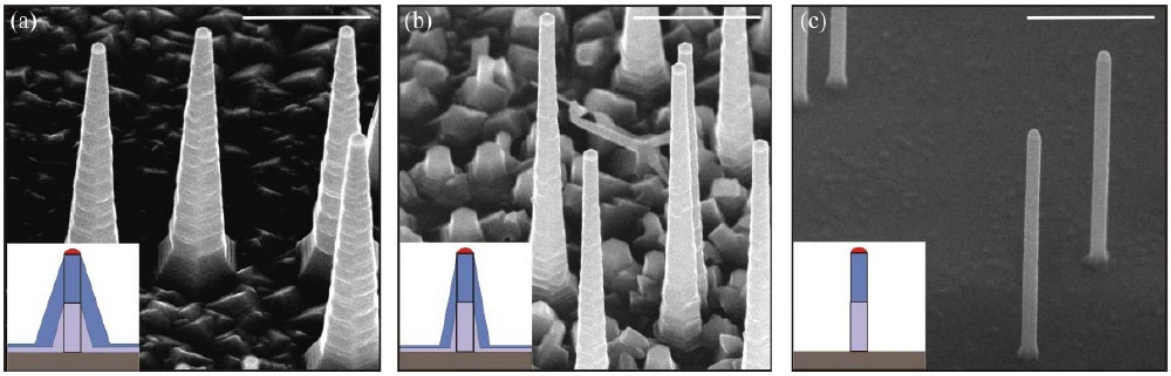

Figure 6: SEM images of in situ etched InP NWs. The nanowires were etched with different amounts of HCl during the growth. (a) reference InP NW, no HCl was added; (b) $x_{HCl} = 1.7.10^{-5}$; (c) $x_{HCl} = 2.9.10^{-5}$. The scale bars represent 1 μm. [17]

An additional etching step with an piranha solution is performed after growth. This etching cleans the nanowire sidewalls. Subsequently the nanowires were covered with SiO_2. This is essential to ensure good adhesion between the nanowires and the chemical isolation and planarization layer benzocyclobutene (BCB). As discussed before SiO_2 also acts as a good passivator for the nanowire surface. Buffered HF is used to etch away the top part in order to make the contact. The structure now is as can be seen in figure 7.

The last step consists of forming the contacts. Ti/Pt/Au is used to form a back

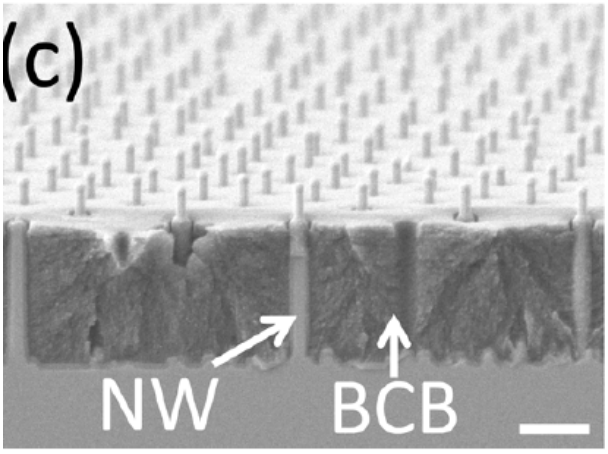

Figure 7: (c)SEM image of the solar cell after etching with buffer HF. [11]

contact on the backside of the wafer. The front contact has to be a transparent metal oxide. As an example figure 8 shows an indiumtinoxide front contact. At the very end the samples are patterned into 500 μm by 500 μm area solar cell devices for optical characterisation.

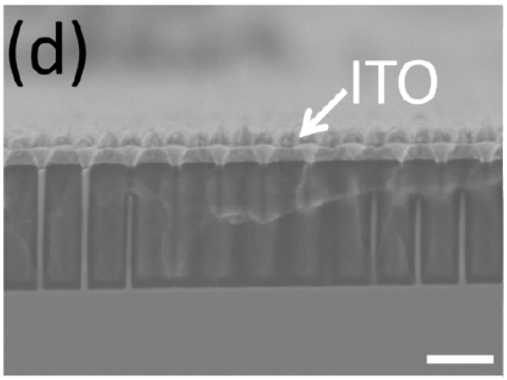

Figure 8: (d)SEM image of the solar cell after completion. [11]

3 Measuring electrical contacts

An excellent TCO should have a low sheet resistance combined with a low contact resistance. We will characterise these two physical properties for the deposited TCOs to be able to compare different TCOs in order to optimise our solar cells. In this section we will first elaborate on the sheet and contact resistance. Afterwards, we will describe the different measurement set-ups. Thereafter, we will elaborate on the deposition and further processing of the samples in order to prepare them for measurements. Finally, the results will be presented and discussed.

3.1 Sheet resistance

In order to measure the sheet resistance we use a four-point measuring technique. This means we use four electrical contacts as will be described below. Furthermore we will derive expressions for the resistivity based on this measurement technique.

We opted for four-point measurements instead of two-point measurements for the characterisation of the sheet resistance of the TCO. Here four electrical contacts are being used. The four-point measuring technique is actually an enhancement of the two-point technique which uses two electrical contacts. Albeit two-point measurements are thus mechanically easier to implement analysing the output becomes more difficult. To see why we will look at the arrangement in figure 9 and elaborate on this difference in the following paragraphs. [18]

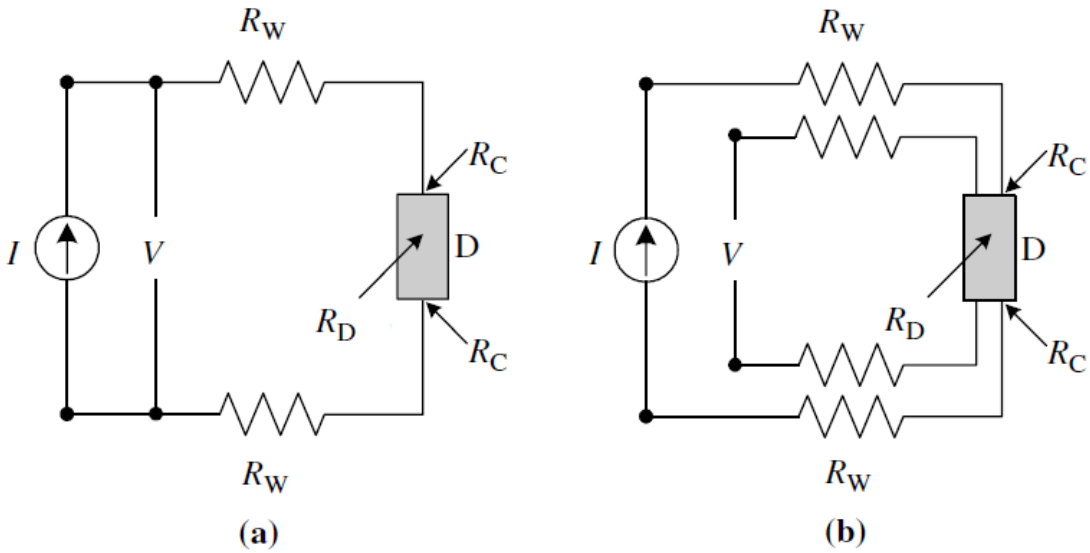

Figure 9: Left: Scheme of the two-point probe method. Right: Scheme of the four-point probe method. D is the device, I the current source, V the voltage probe, R_D, R_W and R_C are the resistance of the device , wire and contacts respectively.

In the left set-up there are two terminals to measure the device (D). Both terminals act as a current and a voltage probe as can be seen in the scheme. The total resistance measured this way is:

$$R_T = V/I = 2R_w + 2R_c + R_D \tag{1}$$

with R_w the resistance of the wire (the measurement probe resistance) and R_c the contact resistance. Since R_w and R_c are not known it is very hard to determine a correct value for R_D. Therefore the four-point measurement technique was developed. Here the probes used for passing the current and measuring the voltage are in two separated paths. The difference now is that the voltage measuring path has a very high input impedance which is a characteristic of the voltmeter. Therefore almost no current flows into this path and as a consequence the voltage drop over R_c and R_w is negligible. The measured resistance is R_D now. Because of the accuracy of this technique four point methods are often used to provide standards for resistivity of thin films. Knowing fundamentally how this technique works we will derive expressions for the resistivity using a four-point measurement and support assumptions using finite element analysis simulations.

The resistivity of a semiconductor material depends on the free electron and hole densities according to the relationship:

$$\rho = \frac{1}{q(n\mu_n + p\mu_p)} \tag{2}$$

Here n and p represent the charge carrier concentrations and μ_n, μ_p their mobility. Although this formula seems to solve our problem immediately, one often does not know the densities and mobilities. As an alternative technique we will be measuring the resistivity using the four-point probe method.

The general set up of a four-point probe is drawn in figure 10. The current is flowing trough tip one and four while we measure the voltage drop between tip two and three. The voltage at point P at a distance r from the probe is given by:

$$V = \frac{I\rho}{2\pi r} \tag{3}$$

In order to justify this assumption we will simulate a basic thin layer of ZnO material and add a point current source ($1e^{-5}A$) to the surface. The result is shown in figure 11. It is clear that there indeed is an $\frac{1}{r}$ dependency but an exact fit is impossible due to the finite number of elements used.
Using formula 3 we can now conduct the voltage at the tip two and three:

$$V_2 = \frac{I\rho}{2\pi}\left(\frac{1}{s_1} - \frac{1}{s_2 + s_3}\right) \tag{4}$$

$$V_3 = \frac{I\rho}{2\pi}\left(\frac{1}{s_1 + s_2} - \frac{1}{s_3}\right) \tag{5}$$

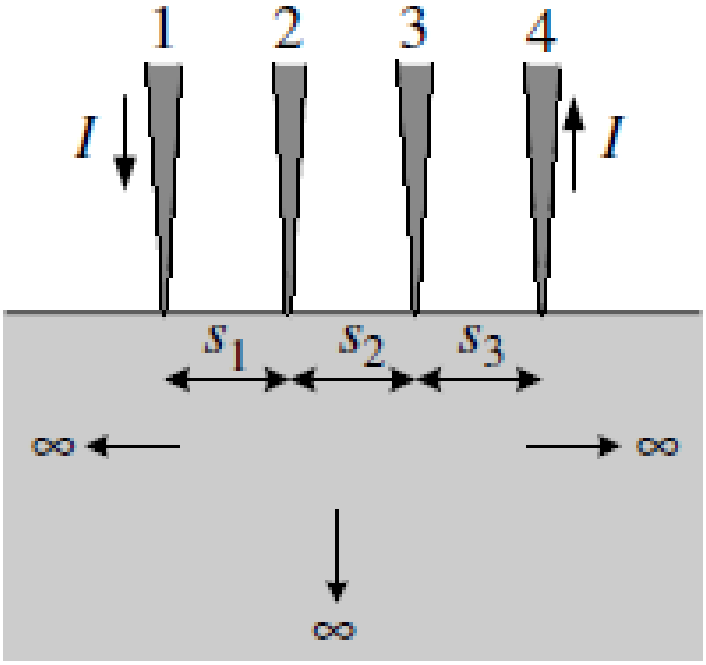

Figure 10: Scheme of the four-point probe method.

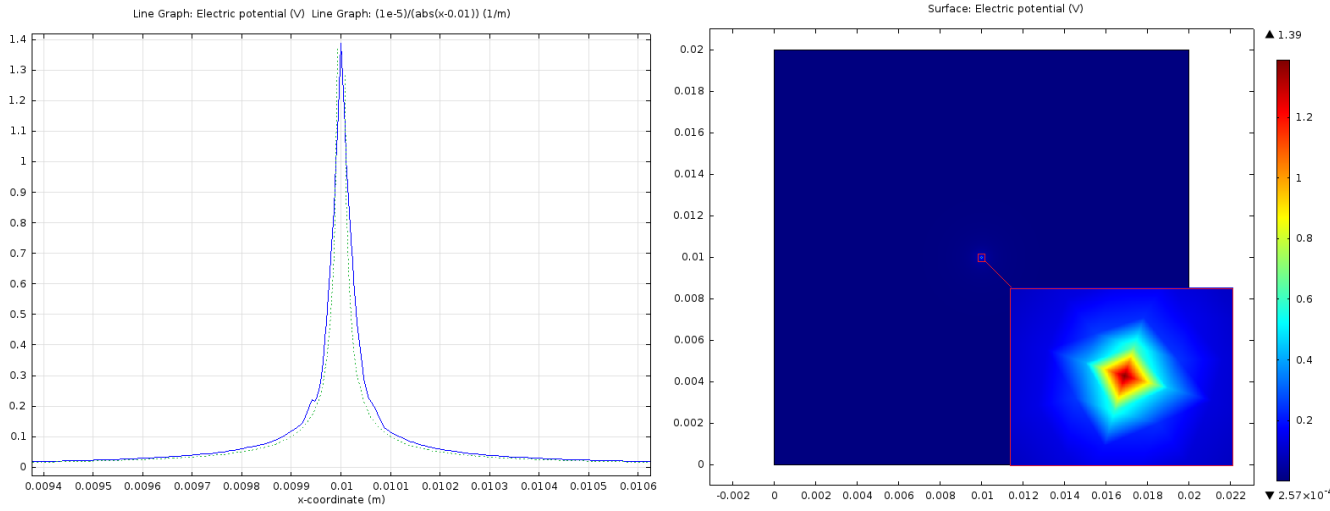

Figure 11: Left: Voltage over a centerline versus distance. The blue line is the simulated value while the green line is a $\sim \frac{1}{x}$ approximation. Note the peaks are not infinitely high because of the finite number of elements. Right: Surface plot showing the top plane of the thin film.

This way the voltage drop between tip 2 and 3 becomes:

$$V_{23} = V_2 - V_3 = \frac{I\rho}{2\pi}(\frac{1}{s_1} - \frac{1}{s_2 + s_3} + \frac{1}{s_3} - \frac{1}{s_1 + s_2}) \tag{6}$$

Which leaves us with an alternative equation for the resistivity:

$$\rho = \frac{2\pi}{1/s_1 - 1/(s_1 + s_2) - 1/(s_2 + s_3) + 1/s_3}\frac{V}{I} \tag{7}$$

The probe station which is being used has one arm with four tips located in a straight line at 1.58 mm separated from each other. The data is recorded trough a current sweep while the voltage is read out by a Labview interface. Equation 7 will then reduce to:

$$\rho = 2\pi s\frac{V}{I} \tag{8}$$

As suggested in Figure 10 this reasoning assumes a semi-infinite surface. Since this is not the case one must use a correction factor donated F:

$$\rho = 2\pi sF\frac{V}{I} \tag{9}$$

The most important correction factor is the layer thickness. According to Masato Yamashita and Mashiro Agu the relation between probe separation (s), sample thickness (t) and the geometrical correction factor is constant for very small values of s and t. This can be seen in figure 12. The model that is used here is the dependence of the resistivity in the form of:

$$\rho = F'(tV/I) \tag{10}$$

In our samples the thickness is tens of nanometres while the probe separation is around 1.58 mm. It is clear we are in the outer left regime and the correction factor can be approximated by $\frac{\pi}{ln(2)}$. The calculation of this is a numerical result based on the conformal transformation method.

The correction factor F, as suggested and confirmed by Shroder, is then:

$$F = \frac{t/s}{2ln(2)} \tag{11}$$

Numerically this gives us a rather simple expression of the resistivity:

$$\rho = 4.532(tV/I) \tag{12}$$

The sheet resistance is then given by:

$$R_{sh} = \frac{\rho}{t} = 4.532(V/I) \tag{13}$$

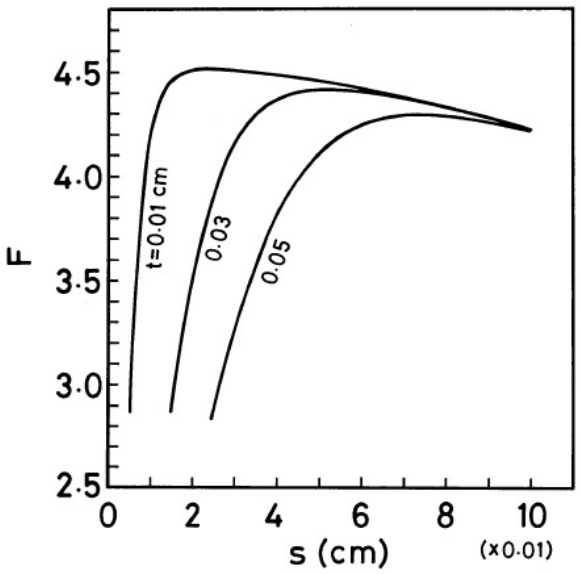

Figure 12: Geometrical correction factor versus probe separation for three different thicknesses. [19]

Practically for sheet resistance measurements the current may not leave the measured thin film. Otherwise the current will flow trough the substrate and its resistance will alter the measurement severely. Therefore the substrate on which the film is deposited should be insulating.

Please note albeit the four-point measuring technique seems superior to the simpler two-point this does not make the two-point measuring technique redundant. First of all the two-point method is mechanically easier to implement. Secondly the probes are often very good conductors which , in most cases, makes R_w almost negligible compared to R_D. Furthermore material wise one can try to minimise the contact resistance by , for example, altering the device with a thin gold layer. We will come to this topic later again when talking about the contact resistance.

3.2 Contact resistance

Measuring the sheet resistance is interesting but does not render a complete image. In most electronic devices, especially solar cells, the contact interface between the metal oxide and the semiconductor plays an important role. We therefore wish to quantify and investigate this contact resistance. Minimising the contact resistance could then possibly increase the performance of solar cells.

The transfer length method, short TLM, provides an excellent approach to measure this contact resistance R_c while simultaneously also providing the sheeth Resistance R_s. The method can applied in the same four-point probe station but requires only two probes due to applying a gold contact layer on the actual contacts.

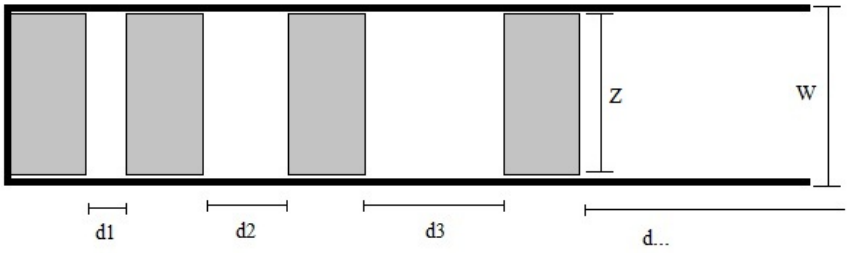

Figure 13: The general outlook of the sample for a TLM measurement.

For the measurement we will need an array of contacts with width Z, length L and different spacing d_i. The setup is shown in figure 13. The theory described in the following paragraphs assumes $|W - Z| << Z$. We will therefore approximate Z by W. The total resistance between any two contacts is given by:

$$R_T = \frac{R_{sh} d_i}{W} + 2R_c \tag{14}$$

This relation comes from the resistors shown in figure 14. The current passes in and out of the contact, which contributes the term $2R_c$, furthermore the resistance in the semiconductor R_{semi} can be expressed as:

$$R_{semi} = \frac{R_{sh} d_i}{W} \tag{15}$$

Plotting R_T For different values d one obtains the typical graph shown in figure 15. It is clear that several parameters can be extracted from the graph. From the slope one obtains the sheetresistance R_{sh} (Z=W is known). For $d = 0$, which is obtained by a linear fit, one obtains $2R_c$. This is logical since this follows directly from equation 14. The intercept on the d-axes gives us the value of L_T also called

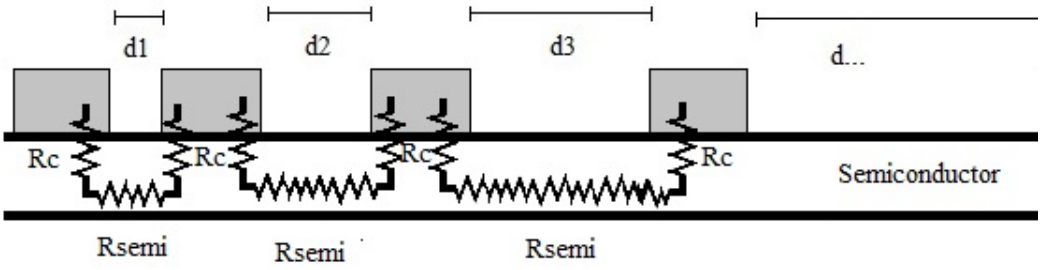

Figure 14: The general outlook of the sample for a TLM measurement indicating the important resistance components.

the transfer length. The transfer length can be calculated as:

$$L_T = \sqrt{\frac{\rho_c}{R_{sh}}} \tag{16}$$

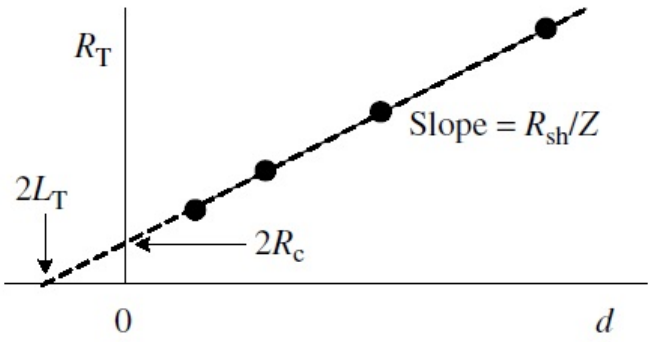

Figure 15: The general outlook of the sample for a TLM measurement.[18]

The value for L_T is characteristic for the way the current flows. The cause is shown in figure 16. This is called the phenomenon of current crowding. The amount of current flowing at the edge is a lot more significant then further away. If x represents the distance from the edge:

$I(x) \sim exp(-x/L_T)$

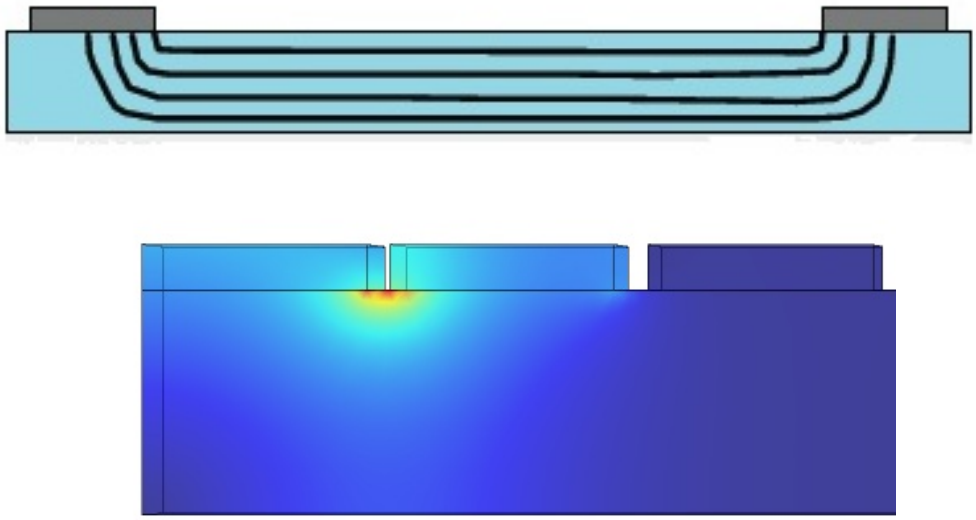

Figure 16: The phenomenon of current crowd. Above is a schematic example (with the contacts in grey and semiconductor layer in blue), underneath is a simplified numerical Comsol simulation of our TLM structure (red corresponds with a high current density, blue with a low current density). [20]

The transfer length is the average distance that an electron travels in the semiconductor beneath the contact. This way one can define an effective contact area: $A_{contact} = L_T W$. Using the definition of the contact resistivity, $\rho_c = R_c A_{contact}$, one obtains:

$$R_c = \frac{\rho_c}{A_{contact}} = \frac{\rho_c}{L_T * W} \tag{17}$$

Using equation 16:

$$R_c = \frac{R_{sh} L_T}{W} \tag{18}$$

We can now rewrite equation 14 as followed:

$$R_T = \frac{R_{sh}}{W}(d + 2L_T) \tag{19}$$

Which proves the physical meaning of the point $R_T = 0$ in figure 15 as discussed before.

Practically we are going to realise a set up as shown in figure 17 inspired by Reading et al. [21], Fisichella et al.[22] and many others. Dimension wise we choose for a TLM pattern consisting eight rectangular contact pads. A typical pad spacing

would be: $10um$, $20um$, ...$100um$.

50 nm titanium and 100 nm gold is used as a top layer for a better contact between the probes and the system. The contact resistance between the metal probes and the gold is thus negligibly small. This ensures us good results using a 2-point probe method as noted earlier in section 3.1. This eases the mechanical complexity of putting the probes on top of the small contacts.

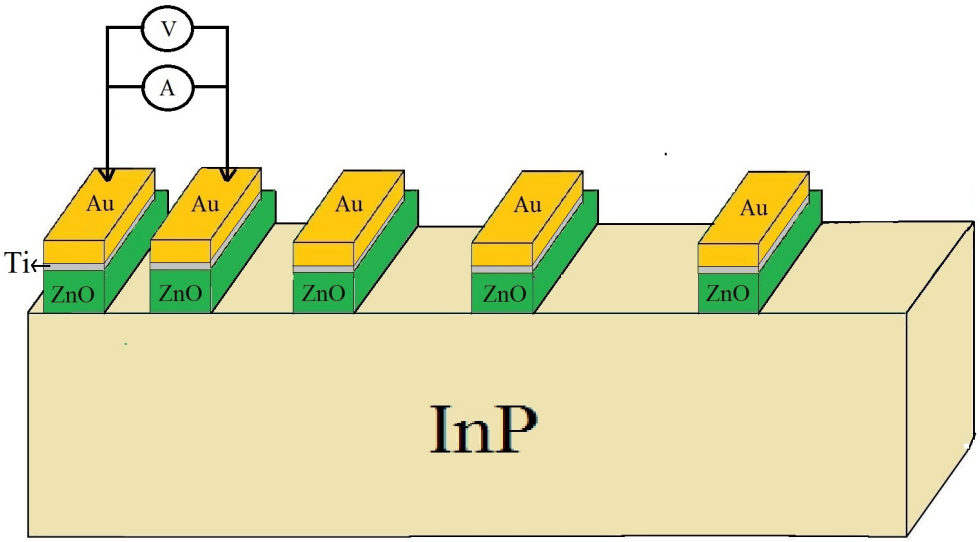

Figure 17: A schematic overview of the sample prepared for TLM measurements.

Alternatively a simplified TLM structure can be formed. This structure consist of very large contact pads which relaxes the requirement of the isolation of the contact structure. This is because the structure becomes so large in at least one dimension that the sample on itself can be seen as isolated. This simplification comes with several advantages. Four-point probe methods become possible because of the larger sized pads, less processing steps are required and more uniformity is achieved.

3.3 Measurement set-ups used for characterisation

In this section we will provide a description of the measurement set-ups being used. Afterwards advantages and disadvantages of each measurement technique is being discussed. Three measurement set-ups are being used in order to have a good understanding of the measurements done.

The main tool for electrical characterisation is a cryogenic probe station of Janis accompanied by Keithly measurement tools. The set up is shown in the left side of figure 18. The ability to cool down and measure in a vacuum is not being used because it has no relevant interest for solar cell applications.

A second important measuring device are two Kleindiek probes. The Kleindiek probe together with an SEM image of a measurement is shown on the right side in figure 18. Both probes are accompanied by a controller for accurate probe displacement. The probes can be used outside using an optical microscope or inside a SEM.

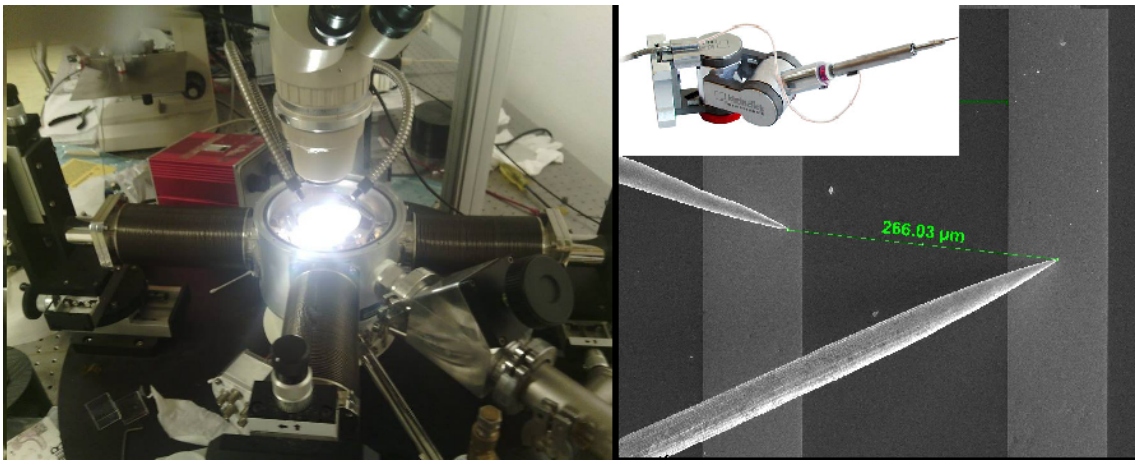

Figure 18: Left: The probestation. Right: The Kleindiek probes.

4 Fabrication of the sample

In order to characterise the sheet resistivity and contact resistance suitable samples should be fabricated. Both sheet and contact resistance ask for a different approach and we will elaborate on this in this section. We will discuss mainly deposition and lithography techniques.

4.1 Deposition of the oxide layer for sheet resistance characterisation

Atomic layer deposition, for short ALD, is a growth process (chemical vapor deposition) that makes it possible to grow ultra thin films. ALD enables us to control the thickness at the subnanometer level. In order to check if the required thickness is reached an ellipsometry measurement will be executed. In this section the ALD process will be described followed by a discussion on the ellipsometry measurement.

The machine used for the atomic layer deposition in this thesis is the Oxford Instruments OpAL^{TM} system. This is an open-load ALD suitable for the thermal ALD (no plasma) being used in this thesis. All oxides we deposited are deposited on a temperature of 125 °C. The system is shown in figure 19 .

Figure 19: The atomic layer deposition machine used in the growth of our samples. The spectroscopic ellipsometry viewports are clearly visible. [23]

Depending on the precursor, atomic layer depostion can deposit different metal oxides. Using ALD intrinsic ZnO and Al doped ZnO were deposited on an InP substrate. The Al doped ZnO was formed by inserting one Al_2O_3 cycle after every n i-ZnO cycles. This constituted one super-cycle. A number of super-cycles were repeated to achieve the desired thickness. All depositions were done on SiO_2 in order to have an isolating substrate as suggested in section 3.1. The samples grown for this project are listed in table 1.

The main idea in this chemical vapor deposition process is a sequence of precursors which are always separated from each other. A purge step has to be taken each time a new precursor enters the chamber. The precursors needed for the deposition of Zn and Al are shown in figure 20 together with an example of the actual recipe used for the AlZnO. The general idea behind ALD, more specific Al deposition, is shown in figure 21. The first step consists of the first precursor reacting with the surface and bonding. When all bonding spaces are used up the chamber is purged. Using a sufficient purge gas reactions between precursors are avoided. In the third step a second precursor (also described as H_2O dose) reacts with the first to form the target material. The residues of this reaction are purged away again in a fourth step. This sequence of steps repeat itself until the required thickness is reached.[24]

Table 1: An overview on the samples grown for further electrical characterisation.

Material	Tickness (nm) (Al:ZnO ratio)	Substrate
AlZnO	50 (1:12 ratio)	InP+SiO
	75 (1:12 ratio)	InP+SiO
	100 (1:12 ratio)	InP+SiO
	100 (1:23 ratio)	SiO
ZnO	50	InP+SiO
	75	InP+SiO
	100	SiO

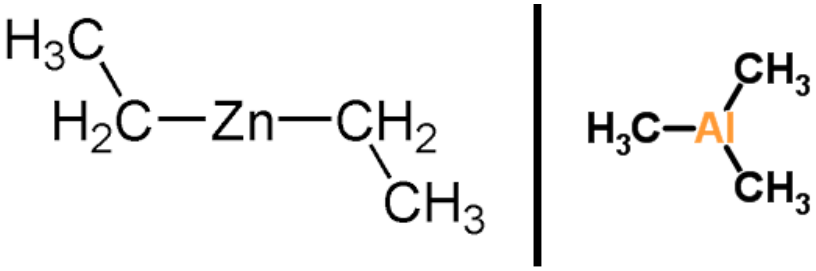

	i-ZnO		Al_2O_3
DEZ dose	50 ms	TMA dose	50 ms
DEZ purge	5s	TMA purge	3.5s
H2O dose	100 ms	H2O dose	200 ms
H2O purge	6s	H2O purge	5s

Figure 20: Zinc precursor (DEZ, diehtylzinc) and aluminium precursor (TMA, trimethylaluminum). Underneath an example recipe is given.

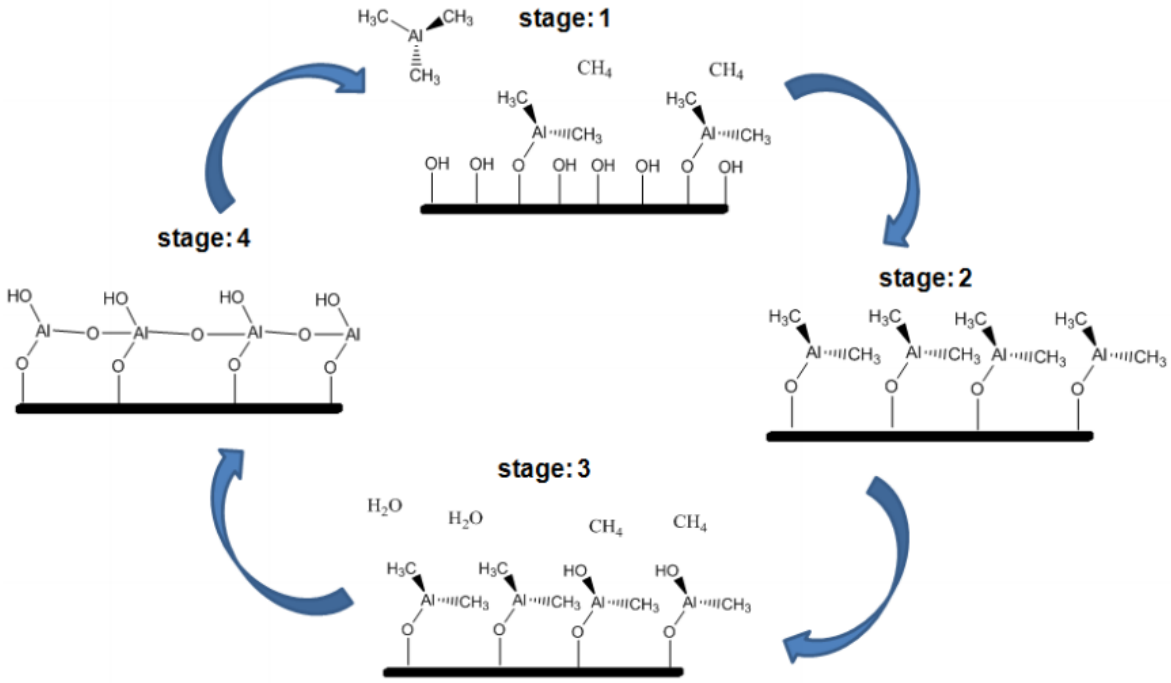

Figure 21: ALD growth cycle includes four stages: 1) Exposure of the first precursor, 2) purge of the reaction chamber, 3) exposure of the second precursor, and 4) a further purge of the reaction chamber. [24]

The recipe alone does not ensure that the growth will be as desired. The growth is very dependable on the substrate. Therefore spectroscopic ellipsometry is performed to ensure that the growth goes as predicted. Spectroscopic Ellipsometry is an optical measurement technique based on the change in polarization caused by interaction of the light with the thin deposited layer and the substrate. The change is determined by the thickness and optical constants of each layer. In order to judge the thickness experimental data is compared to a theoretical model. From this model a best possible fit is made from which the thickness can be deduced. [25] As an example figure 22 shows the result obtained in the ellipsometry measurement of one of our samples.

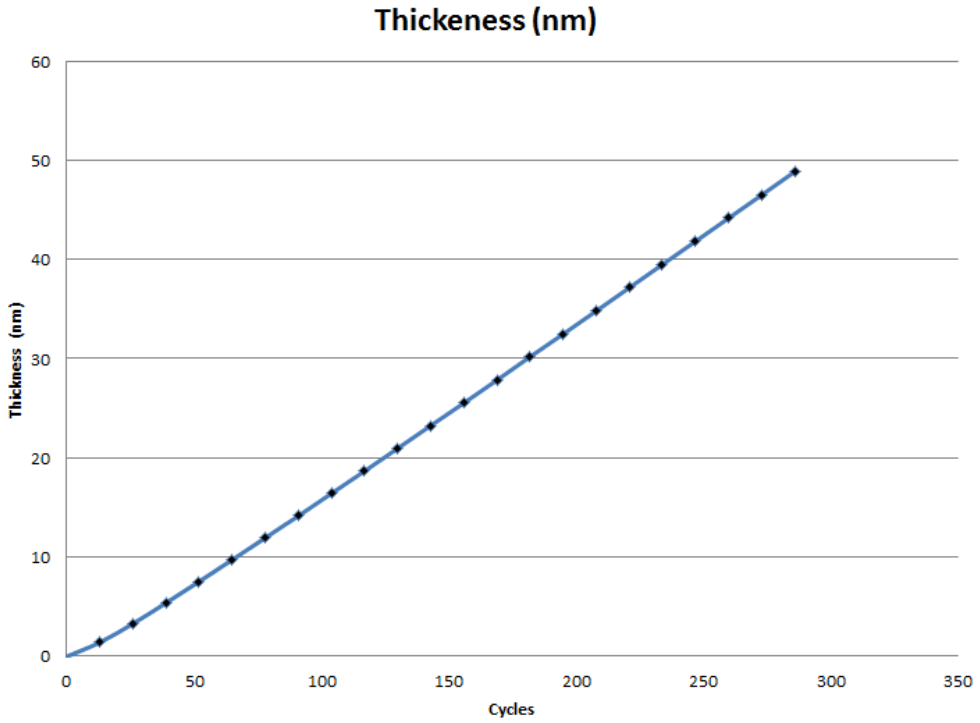

Figure 22: Thickness versus the number of passed cycles measurement using ellipsometry. [24]

4.2 Fabrication of the TLM structures

Constructing the TLM structure consists of multiple steps on which we will elaborate below. The most important technique used is the optical lithography using the KarlSuss MA-6 Aligner. We will start the processing with the samples obtained by atomic layer deposition as described in the previous section. However this time we will use InP as a substrate. The process consists of two major parts: creating a mesa and creating the contacts. Both will be done by a cleaned mask suited for TLM structures. After the process energy dispersive x-rays spectroscopy, EDX, is used to review the structure.

It is important to notice that clean samples are extremely important for an accurate determination of R_c. Any oxidation or dust particles might influence and make the contact resistance more variable and thus the TLM measurement interpretation more difficult. To reduce this effect it is advised to do the atomic layer deposition and the construction of the TLM measurement sample sequentially.

First of all we will start depositing a 100 nm layer of SiN and spin (2000 RPM, 30s) the positive photoresist HPR 504. Large samples have a more uniform spinning of the photo resist. This thus reduces edge effects on the sample and more TLM structures are available for measurement. A positive photoresist will make the resist that is exposed to light soluble to the photoresist developer, in this case the OCG developer (1 minute) is used. The program for the optical lithography consist of 7 seconds exposure in vacuum contact. Large samples ensure a good vacuum contact which results in a high resolution. During these steps three baking steps are done: one after spinning, one after exposure and one after development during 2.5 minutes at 100°C 115°C and 120°C respectively.

Afterwards the SiN reactive ion etching etches 100 s while the HPR is used as a mask. This mask is afterwards removed by 10 minutes bathing acetone and three minutes in a polymer stripper. Diluted HCl (0.36%) is now used to etch away the zinc oxide during a small time step of 20 seconds while the remaining SiN is used as a mask. Now the mesa is formed by etching the InP with a mixture of H_3PO_4 and HCl (an 80:20 ratio during 1 minute to etch 4 micron). In the end wet echting with buffered HF or dry etching, the SiN reactive ion etching, is used to remove the remaining SiN. A general overview of the different steps to create the mesa can be found in figure 23.

To form the contacts a negative resist MAN 440 is applied (2000 RPM, 30s). This type of photoresist will become insoluble to the photoresist developer where it was exposed to light. After the spinning one baking step of 5 minutes on 95°C is required. The optical lithography program consists of three exposures of 111 seconds with a 10 second wait in between in vacuum contact. The development is done with MAD-332s during 4 minutes.After the optical lithography the metal deposition follows. 50 nm of titanium followed by 100 nm of gold is evaporated on the surface. A simple lift off process is now done to remove the Man 440 with a

short bathing in acetone, the gold layer on top of the resist will also be removed by the process. In the final step diluted HCl (0.36%) is now used to etch away the zinc oxide during a small time step of 20 seconds as previously also done while making the mesa's. A general overview of the different steps to create the contacts can be found in figure 24.

An alternative and more simple structure can also be formed as already suggested in the previous section. Less and simpler processing is required albeit the approach is similar to the regular TLM structure. This time we start with the negative resist MAN 440. The lithography is done with the mesas of the previous TLM mask. Now the the Ti/Au deposition and a lift off process is applied to be left with contacts as large as the mesas with the ZnO still in between the contacts. Conform with the previous process HCl is being used to remove the ZnO in between while the gold is used as a mask for the ZnO in the contacts.

In order to have any idea whether the structure formed as expected, energy dispersive x-rays spectroscopy, EDX, is applied to different regions in the sample. EDX is used for an element analysis based on an x-ray excitation source, electrons, and the emission of the sample. [26] The results, of an intrinsic ZnO sample made by the alternative method, are shown in figure 25. The structures show the behaviour as expected. Between the pads only peaks of the In and P are coming from the substrate. The pads themselves have an extra contribution from the Au, Ti and Zn.

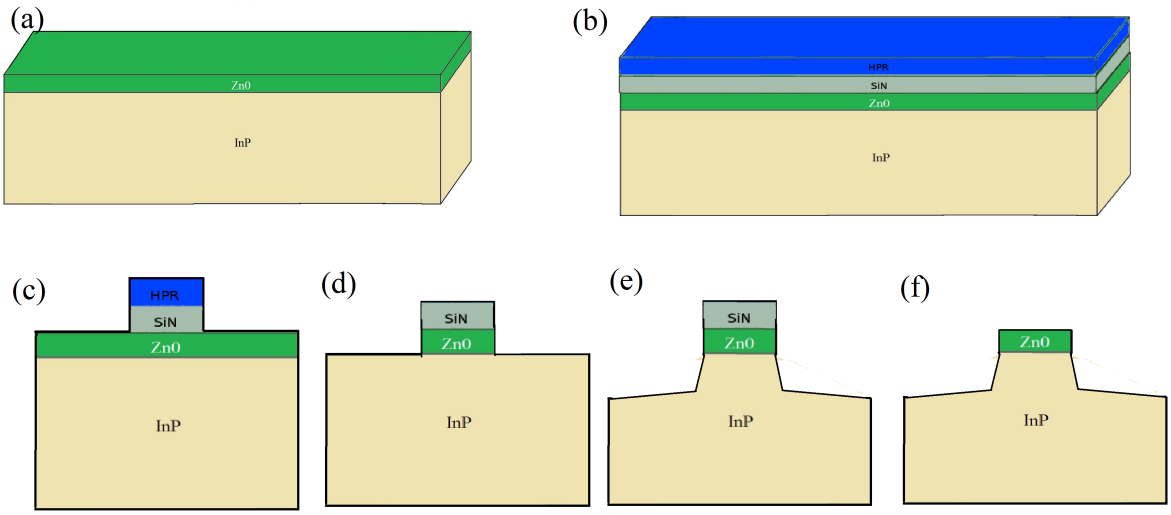

Figure 23: (a) The starting point by ALD. (b) Adding SiN and resist layer. (c) After optical lithography and SiN-etching. (d) Removed resist with acetone. (e) Etching the InP (f) removing the remaining SiN.

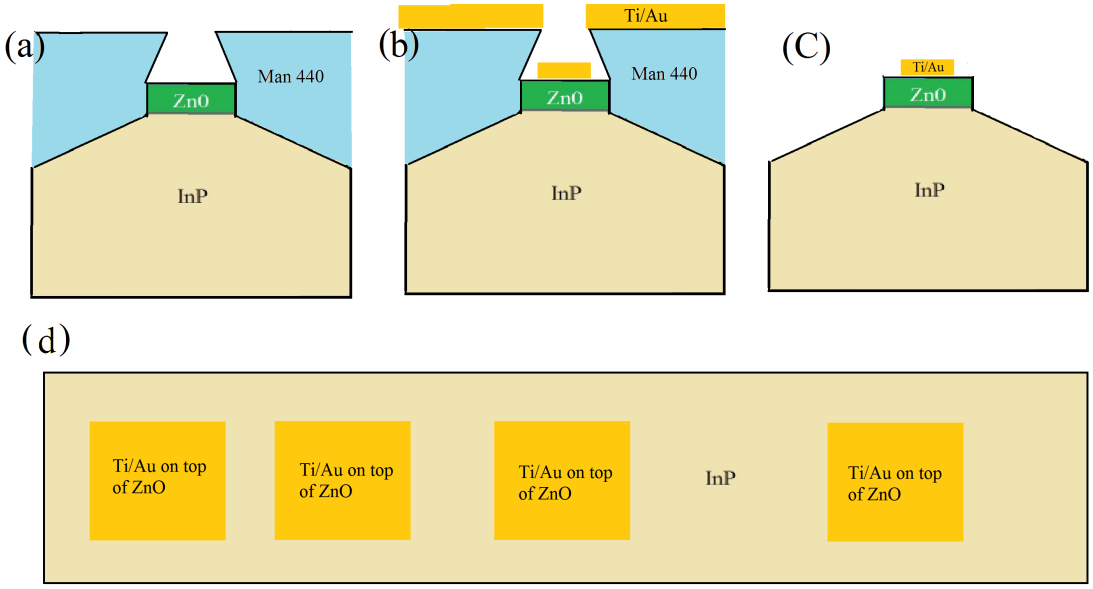

Figure 24: (a) The structure after optical lithography with the negative resist. (b) After metal deposition. (c) After the lift off process. (d) After the final ZnO etching step.

Etching times also influence sideways etching of layers even when they are protected by a mask. This effect can often be seen simply by using an optical microscope as can be seen in figure 26 . Multiples samples of the same kind would enable us to produce better and better structures. Because of the open load system this takes no extra efforts but ensures better results.

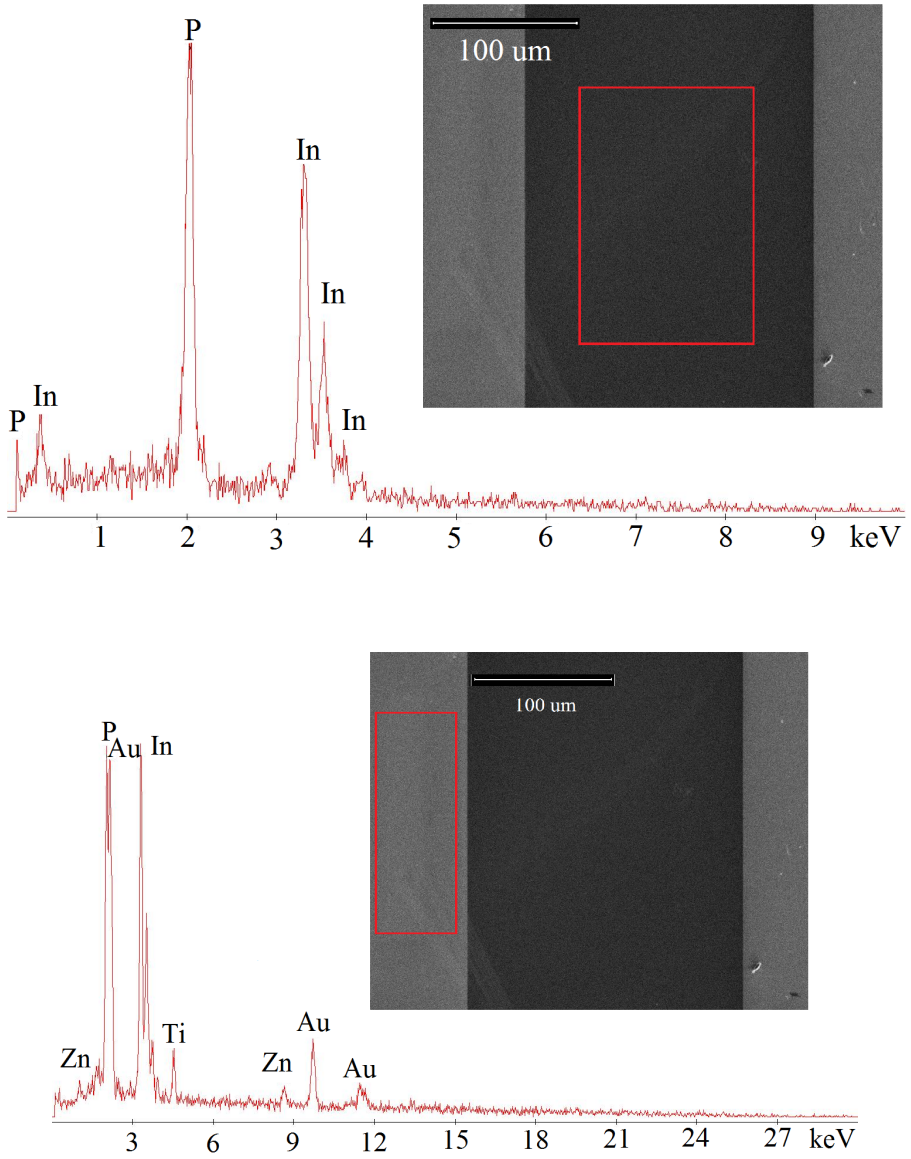

Figure 25: Upper:EDX measurement of the area between the contacts. Lower:EDX measurement of the area on the contacts.

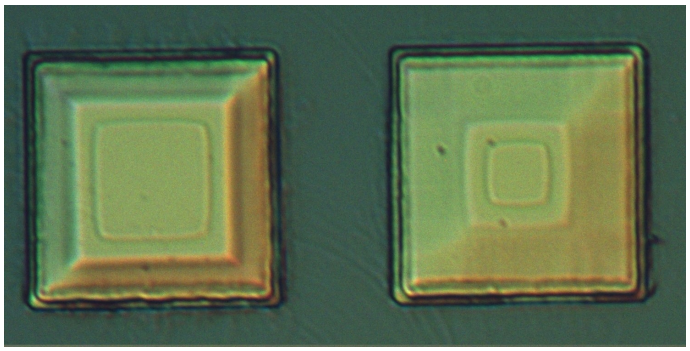

Figure 26: Underetching visible under an optical microscope.

5 Characterisation of the transparent contacts

To characterise the contacts we will investigate the sheet resistance and contact resistance as described in section 3. Expressions derived in the theory will allow us to calculate the quantities of interest which will be presented and discussed.

5.1 Analysis of sheet resistance measurements

The probe station set-up has been described in section 3.3. We will use a four-point measuring technique to measure the sheet resistance as described in section 3.1. Measurements are performed on the metal oxide layers grown on the insulating substrate as listed in table 1 in section 4.1.

Raw data obtained from these measurement are typical linear I-V characteristics. These graphs can be seen in figures 36 till 39 in the appendix. The values of the resistances found are given in table 2. Given these I-V characteristics formula 12 allows us to calculate the resistivity for the different materials. This calculation is performed and the results are presented in figures 43 and 44 from the appendix. An overview is given in table 3. Because the resistivity is thickness dependent it is very interesting to compare these values relative to the thickness. Therefore formula 13 has been deduced to calculate the sheet resistance. This value, in Ohm/sq, allows us thus to make a better comparison between materials. The results are presented in figure 45 from the appendix. An overview is given in table 4.

Scaling of the resistance with the thickness of the metal oxide can be observed in table 2. For bulk material we expect a linear dependency on the thickness but this is not the case here. Clearly these thin film resistances are greatly influenced by the lattice matching with the insulator.

Since resistivity, here expressed in Ωm, is material characteristic ideally different thickness's should have the same resistivity. As can be seen from table 3 this is not entirely true for thin films although they are in the same order of magnitude. This is due a combination of the following effects. The electrical resistance in a metal thin-film arises due to electron scattering by phonons, electron scattering by the surface, point defects, impurities, grain boundaries, film surfaces and interfaces. [27] Because each sample has its own growth recipe other types of defects will occur.

It is clear that the measured sheet resistances of AlZnO are a bit lower than the intrinsic ZnO. The AlZnO with an 1:23 ratio however lowers the sheet resistance greatly an shows thus a more ideal doping. We conclude that doping lowers the resistance but in the case of a 1:12 ratio more lattice scattering is present compared to a more ideal 1:23 ratio. However this value is still rather high compared to the more usual indium-tin oxide (ITO) films for solar cells. Here resistivities of

7.5 E−6 ($\Omega.m$) and 1.3 E−6($\Omega.m$) have been reported.[28][29]

To summarise our findings AlZnO has generally lower sheet resistance than the intrinsic ZnO. Furthermore much improvement can be made considering the doping level to provide an excellent conducting TCO. Anyways all resistivities measured are sufficiently low because the dominating term for power loss will come from the contact resistance.

Material	Tickness (nm) (Al:ZnO ratio)	Resistance (Ohm)
AlZnO	50 (1:12 ratio)	2.0779 E3
	75 (1:12 ratio)	7.7209 E2
	100 (1:12 ratio)	5.0625 E2
	100 (1:23 ratio)	8.1443 E1
ZnO	50	2.8152 E3
	75	1.0847 E3
	100	6.5939 E2

Table 2: The measured resistances for the different materials considered.

Material	Thickness (nm) (Al:ZnO ratio)	≈ Resistivity (Ohm.m)
AlZnO	50 (1:12 ratio)	4.72 E-4
	75 (1:12 ratio)	2.6240 E-4
	100 (1:12 ratio)	2.29 E-4
	100 (1:23 ratio)	3.67 E-5
ZnO	50	6.38 E-4
	75	3.68 E-4
	100	2.99 E-4

Table 3: The measured resistivities for the different materials considered.

Material	Thickness (nm) (Al:ZnO ratio)	≈ Sheat resistance (Ohm/sq)
AlZnO	50 (1:12 ratio)	9417
	75 (1:12 ratio)	3498
	100 (1:12 ratio)	2293
	100 (1:23 ratio)	367
ZnO	50	12762
	75	4913
	100	2988

Table 4: The measured sheet resistances for the different materials considered.

5.2 Analysis of contact resistance measurements

5.2.1 Charactersation of titanium contacts on InP

First we measured the bare InP using the four-point technique of section 3.1. Raw data measured was hard to interpret which led to the conclusion that the contact resistance with the probes dominated our measurement. To verify this an array of gold mesas was formed on the bare InP using a similar method as described in section 4.2. Using a four-point technique the mesas were measured leading to the raw data shown in figure 46 in the appendix. From this data we construct the characteristic TLM graph shown in figure 27. It is clear that there is no trend visible in the data. This implies that the contact resistance between the titanium and the InP dominates over the resistance of the InP wafer. We also expect the same behaviour in further measurements of the contact resistance of ZnO contacts.

Using formula 17 we can calculate the contact resistivity. The linear fit is practically parallel with the distance axis and thus cuts it at large negative value. The theory of section 3.2 then implies that L_T is the whole width of the contact. Again this is due to the low resistance of the InP. A calculation offers a contact resistivity of 9.7x10$^{-5}\Omega cm^2$. This value is lower than $10^{-3}\Omega cm^2$ and thus considered a little low.

Figure 28 shows that the titanium forms an ohmic contact with the InP. This combined with its low contact resistivity makes titanium a good contact material however it has not the transparent property of a TCO.

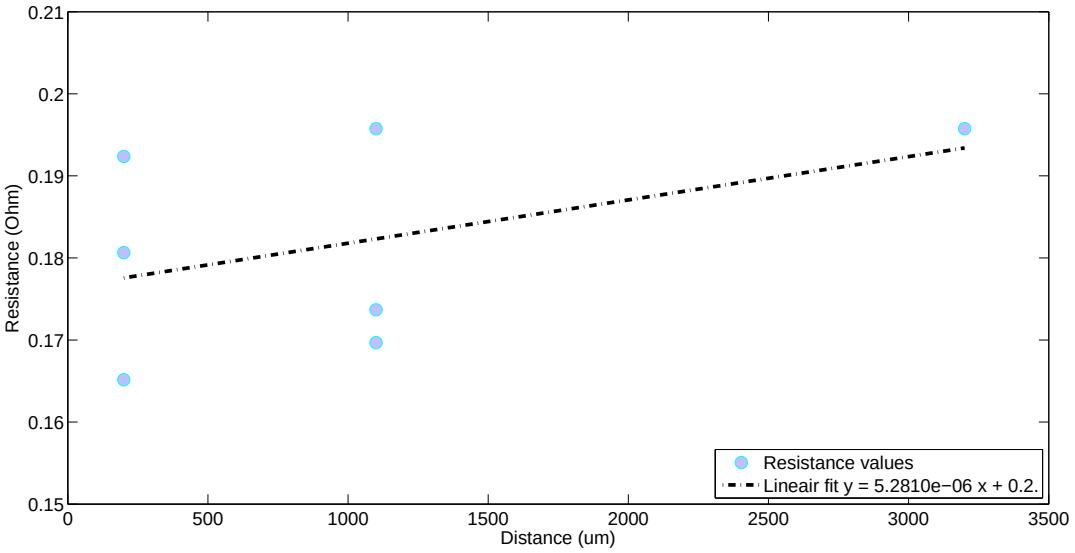

Figure 27: Characteristic TLM graph for bare InP with golden mesas.

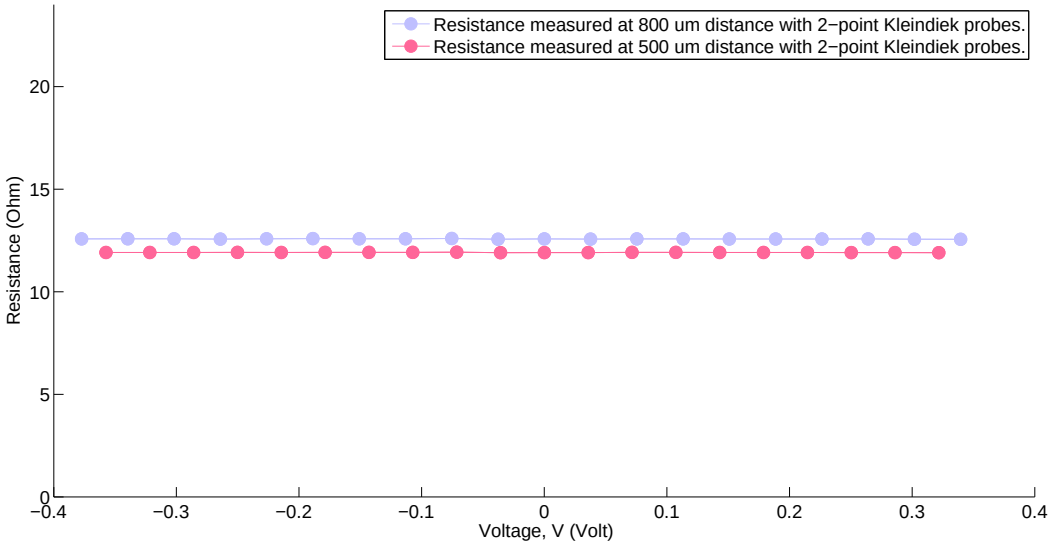

Figure 28: Resistance to voltage plot showing the ohmic relation between the Ti and the InP.

5.2.2 charactersation of (Al)ZnO contacts on InP

We will now present the results of further measurements of ZnO contacts. The samples used are the ones with an InP substrate listed in table 1 and processed as described in section 4.2. Since the contacts were non-ohmic we opt to show the resistances around 0V. The results are shown in figures 29 and 30. The non ohmic behaviour is shown in figures 31 and 34. We calculated the contact resistivities and summarised them in table 5.

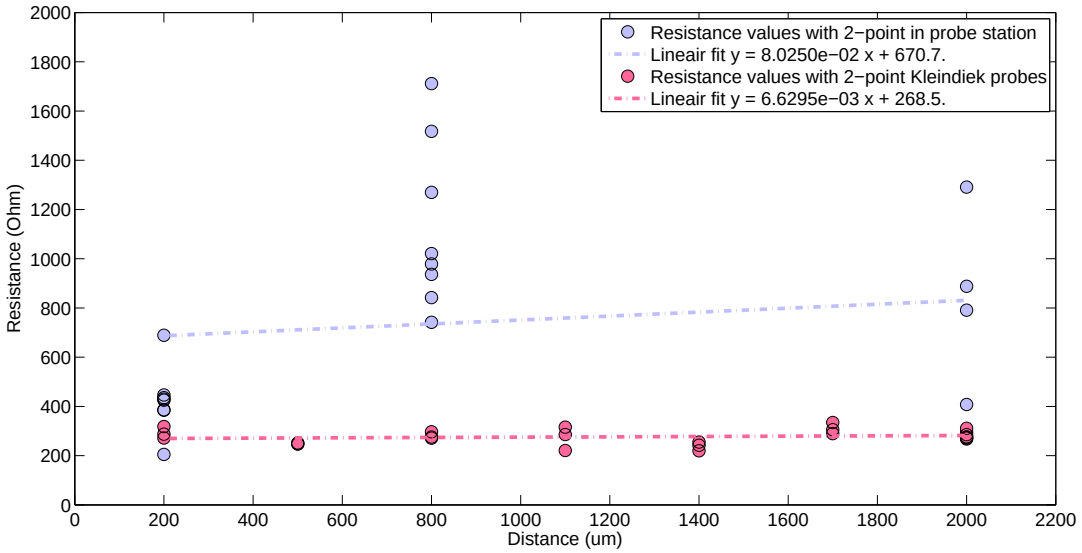

Figure 29: Characteristic TLM graph for AlZnO (1:12) with a thickness of 100nm.

Contact material	Contact resistivity Ωcm^2
AlZnO 100nm	$1.34x10^{-2}$
intrinsic ZnO 50nm	$6.0x10^{-4}$
intrinsic ZnO 75nm	$3.08x10^{-4}$
Titanium	$9.7x10^{-5}$

Table 5: Overview of the contact resistivity for the different materials measured.

It is clear the contact resistivity of intrinsic ZnO is much lower than the contact resistivity of AlZnO. Therefore for solar cell application AlZnO contacts are a significant factor of power loss.

A possible explanation for the high contact resistivity lies in the recipe used for the atomic layer deposition. Dependable on the recipe of the ALD it could be that when depositing AlZnO the first layer is an Al layer. The contact resistance is heavily influenced by the interface layer. This means that an Al interface layer would show a very different characteristic than a ZnO interface layer, which is the

only type of layer present in a intrinsic ZnO film.

Another point of interest is that the the contact of AlZnO, shown in figure 31, and intrinsic ZnO, shown next section in figure 34, is non-ohmic. This is unwanted and a result of the Schottky contact formed between the InP semiconductor and the ZnO metal.

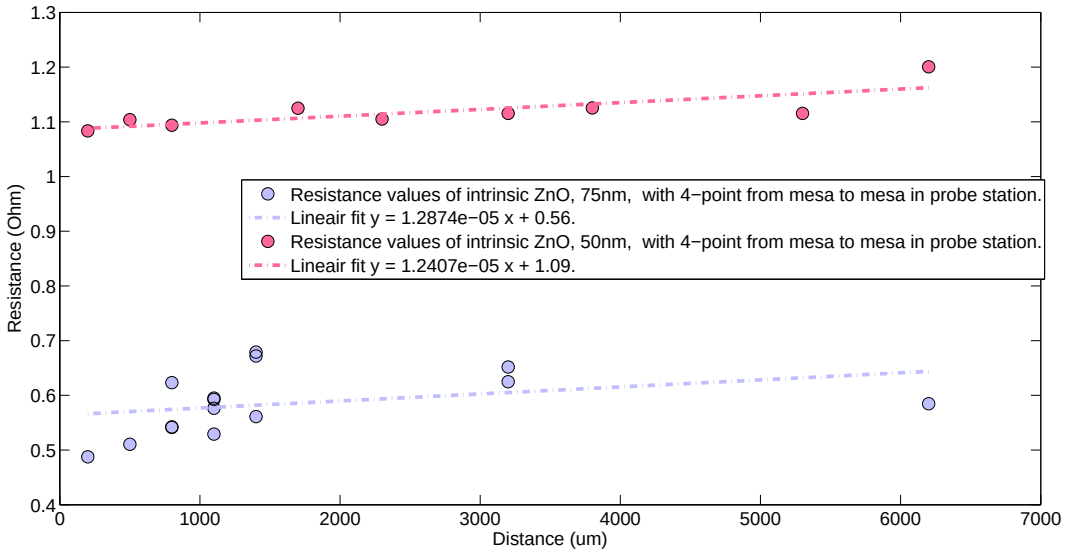

Figure 30: Characteristic TLM graph for intrinsic ZnO with thickness of 50 and 75nm.

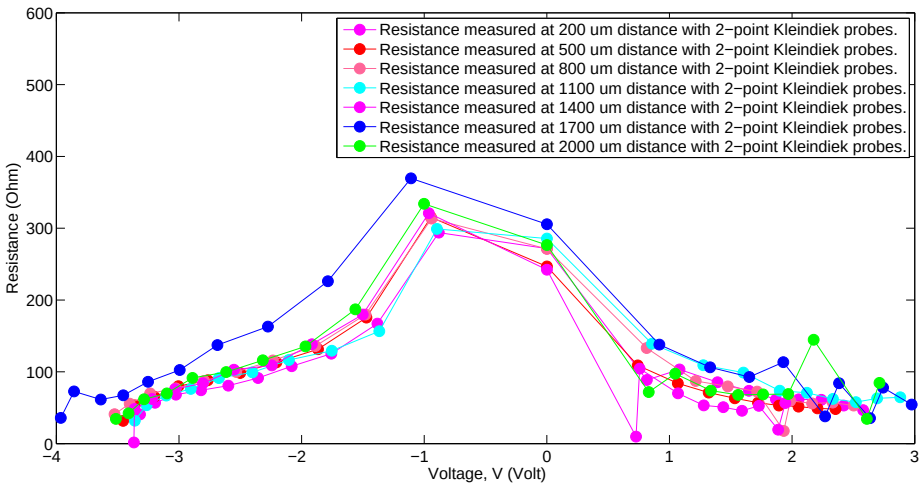

Figure 31: Resistance to voltage plot showing the non-ohmic relation between the AlZnO and the InP.

5.2.3 Verification of low contact resistance of intrinsic ZnO.

A possible cause for the low contact resistivity is the fact that an under etch, as warned for in section 4.2, etched sideways the ZnO which allowed the Ti to make contact with the InP and hence lowers the contact resistance. To confirm the low contact resistivity of intrinsic ZnO measured before we will do a reference two-point measurent with the Kleindiek probes. This time we will use a focussed ion beam (Ga ions) and cut two small pads out of a large mesa. The pads are located in the center of the mesa and thus have to contain a layer of ZnO. The created pads are shown in figure 32.

Measurements are performed and the data is shown in figure 34. The resistance of the probes is also measured by short-circuiting them and amounts 12 Ohm. Furthermore there is also the contact resistance between the probes (tungsten) and the golden top-layer. This taken in account we can still conclude that the resistance measured is not in full agreement with what was previously found since the pads are now much smaller (more than 10 times) and the resistance should be going up a lot.

To further investigate what this conclusion means we set-up a FEM model in order to verify the measurement. For this we will need the conduction of the InP substrate. To quantify the order of magnitude of the conduction of the InP we set-up a FEM computer simulation of the measurement in section 5.2.1. We observed that around a conduction of 3E5 S/m the InP substrate has no significant impact on the measurement. Simulations showing the significant effect of the InP substrate at 1E4 S/m and no significant effect at 3E5 S/m are presented in figure 33. Remark that the current of $\approx$ 6 E-3 mA has been found at a conduction of 3E5 which corresponds to the raw data of figure 46 in the appendix .

Given the conduction of InP now, we can set up a FEM model for the reference measurement shown in figure 34. We choose the contact resistivity based on the two-point Kleindiek probe measurements (figure 34) and based on the 4-point measurement (figure 30) and use those values to generate two models for each geometry shown in figure 32. This simulation is shown in figure 35. It is clear that according to the contact resistivity of the four-point measurement the resistance found should be one order of magnitude higher. Possible explanations for this could be that we damaged the sample doing the four-point measurement beforehand or using the focussed Ga ions. In any case the value of the contact resistance is even lower measured with the Kleindiek probes and intrinsic ZnO still stands as a having a low contact resistivity.

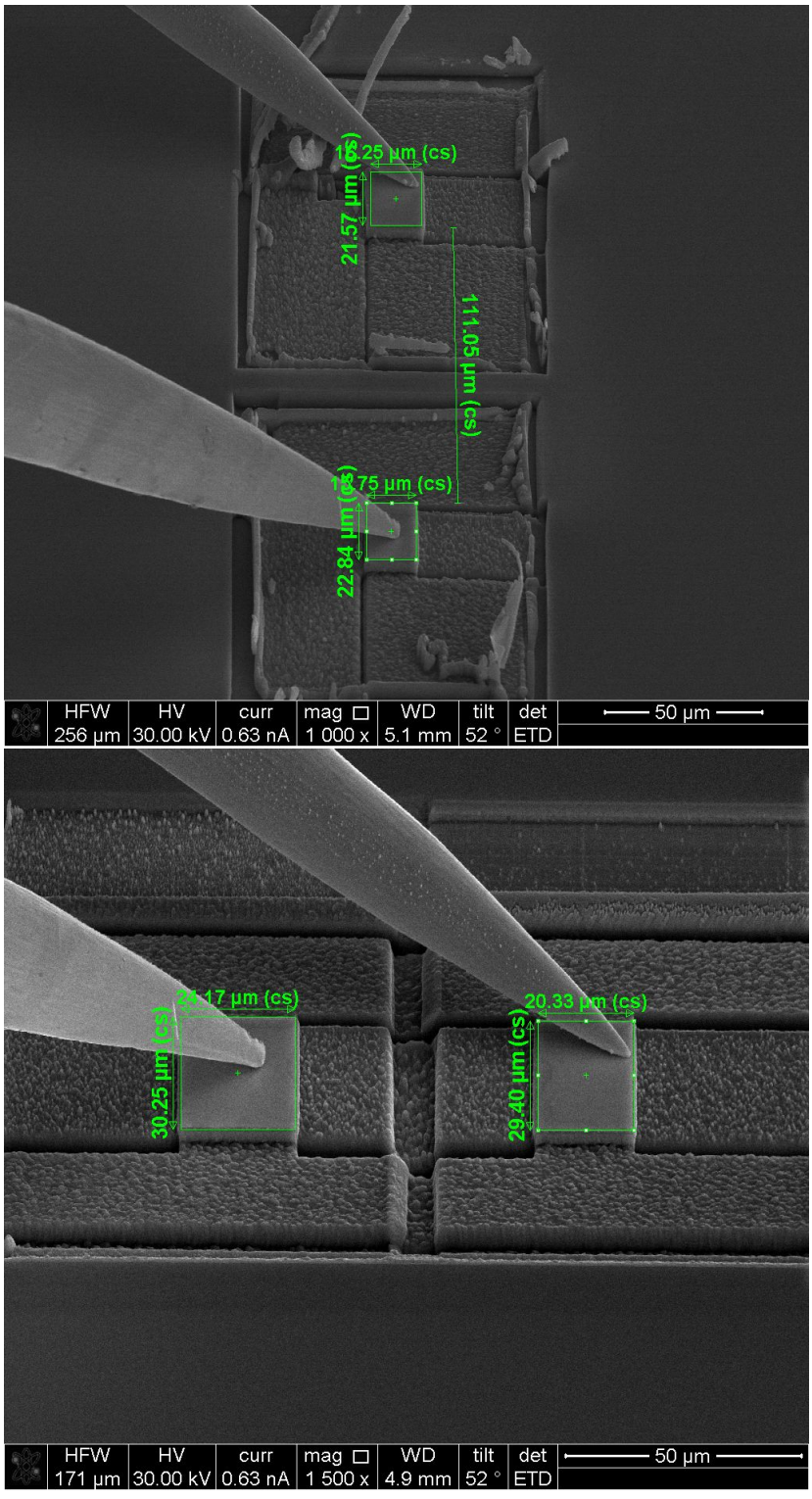

Figure 32: Upper: Pads made on intrinsic ZnO with a thickness of 50 nm. Lower: Pads made on intrinsic ZnO with a thickness of 75nm.

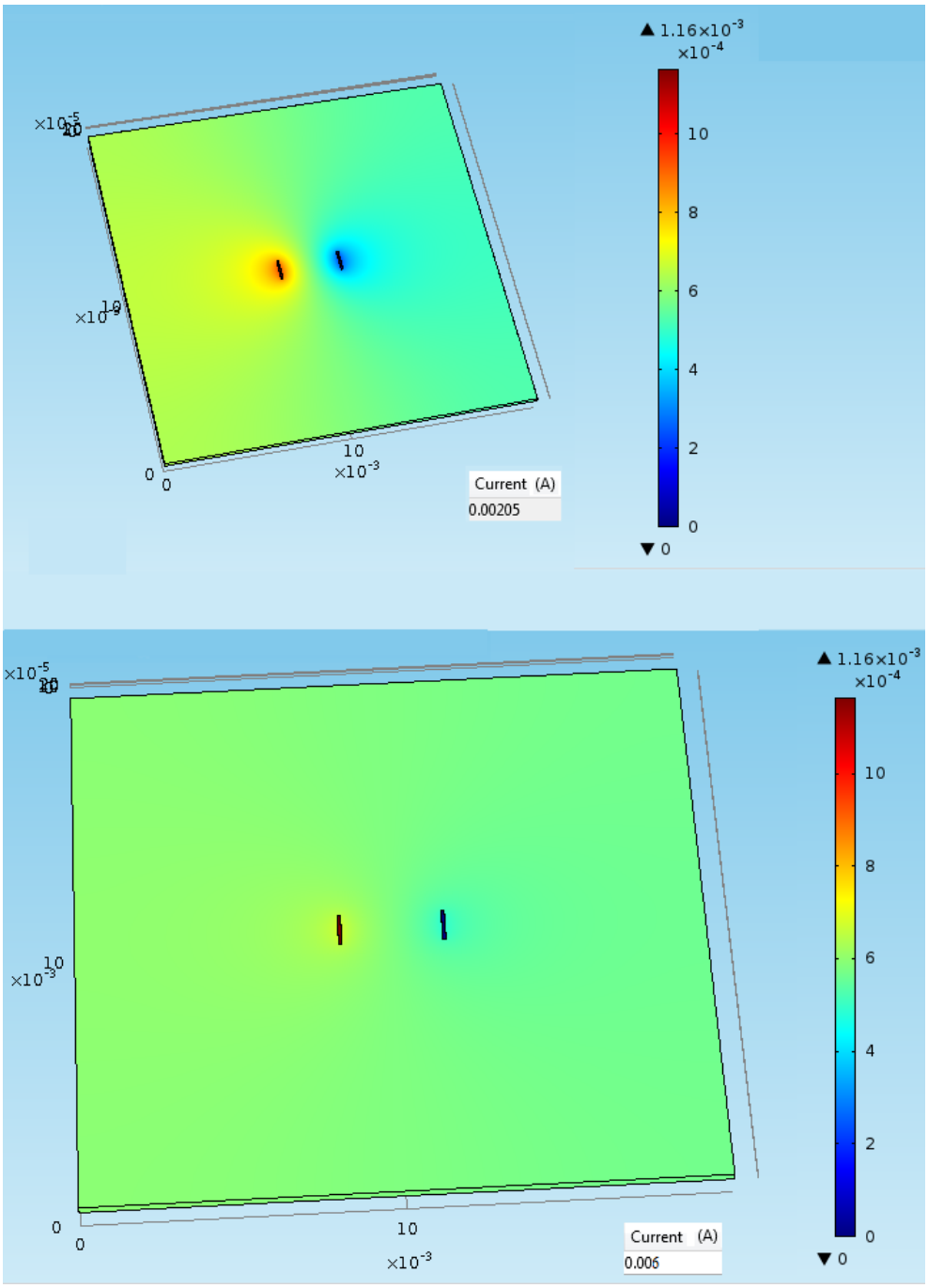

Figure 33: Simulations to determine the conductivity of the InP substrate. Above a voltage plot with a conductivity of 1E4 S/m (big substrate contribution) and underneath a voltage plot with a conductivity of 3E5 S/m (almost no substrate contribution). The latter case corresponds to what has been observed in measurements and renders a current of 6 E-3 mA which has been found in the raw data of figure 46.

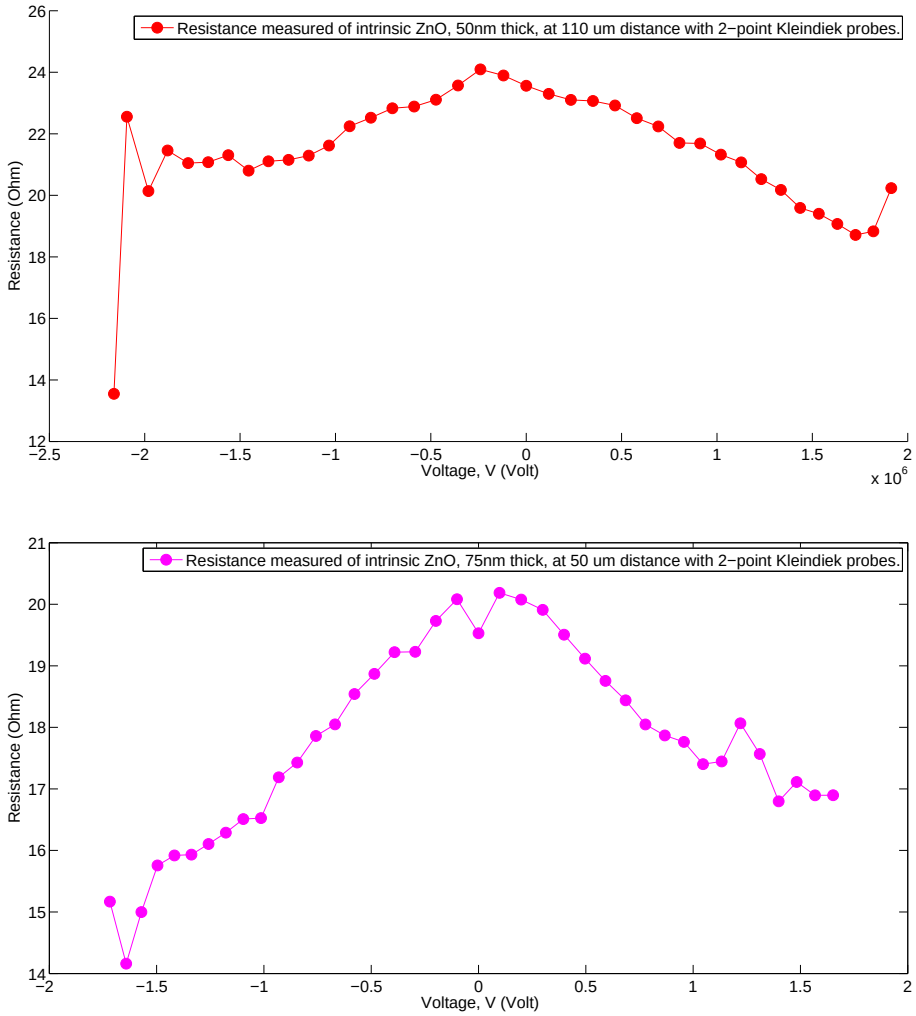

Figure 34: Voltage to resistance plot showing the non-ohmic relation between the 50 (upper) and 75 (lower) nm thick intrinsic ZnO and the InP.

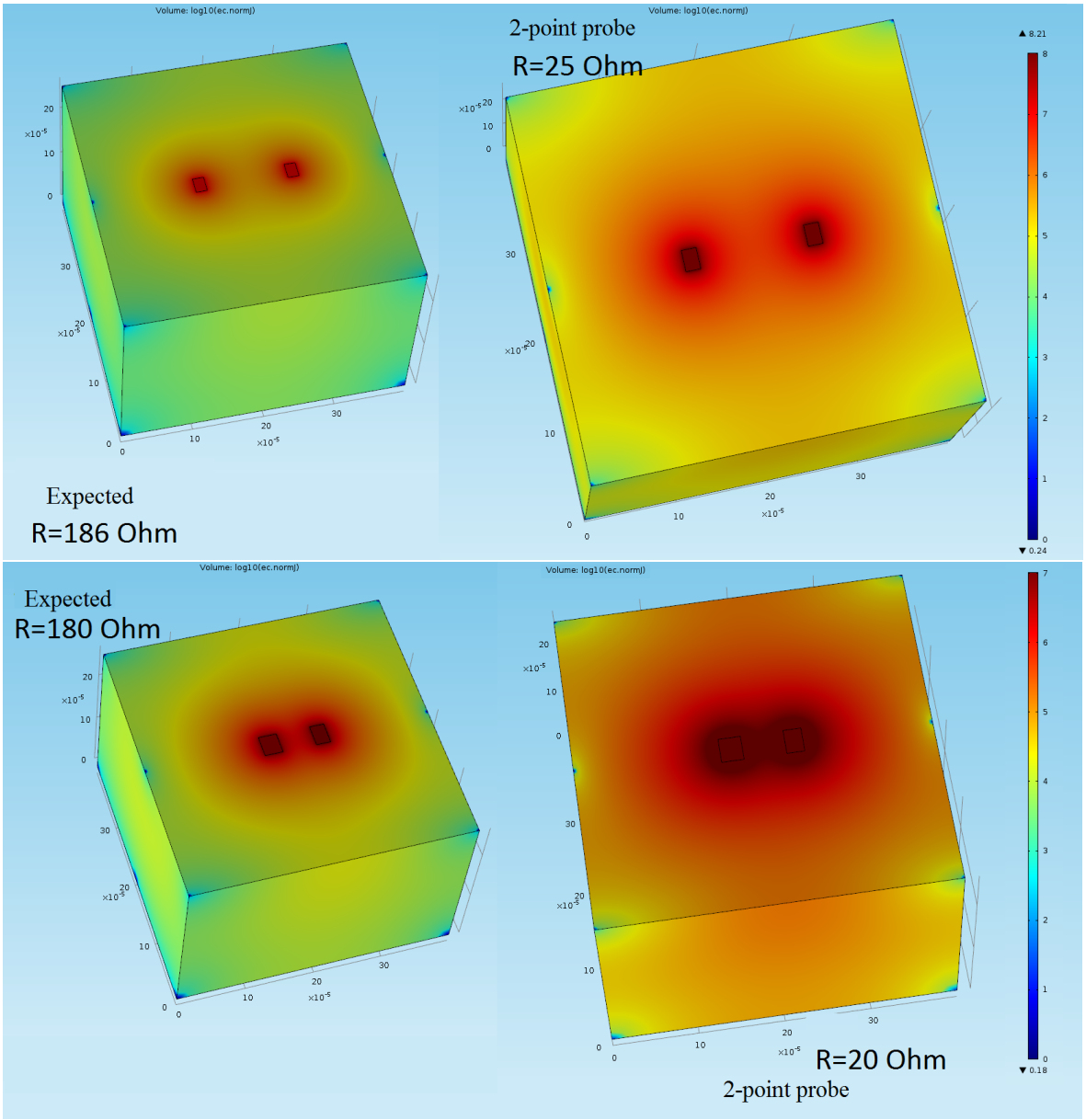

Figure 35: Simulations (all logarithmic current density plots) to check the consistency of the raw data of figure 34 with the contact resistivities earlier reported in table 5. Left are the expected resistances and right the measured resistances of the 50nm (upper two figures) and 75nm (lower two figures) thick intrinsic ZnO.

6 Summary

We have measured the thin film resistance of (Al)ZnO and its contact resistance to InP. These proporties are of great importance to minimise the power loss in our solar cell devices. We observed that the thin film resistivity of AlZnO is significantly lower than intrinsic ZnO. For AlZnO a lowest value of 3.67 E−5 ($\Omega.m$) was reached, which is worse than the commonly used ITO. This is no major problem because the most significant source of power loss in our devices comes from the contact resistivity. Therefore the thin film resisivities measured are sufficiently low.

We found that intrinsic ZnO has a lower contact resistivity with InP than AlZnO. The lowest contact resistivity reached is 3.08x10$^{-4}\Omega cm^2$ which is not significant for power loss within the solar cell. We thus conclude that it is possible to minimise power loss within the solar cell using intrinsic ZnO TCOs.

Computer simulations have shown that measurements in different set-ups, likely due to damaging the sample, show different results. The conclusion for intrinsic ZnO as good contact material however remains the same.

In conclusion: Intrinsic ZnO is a potential solar cell contact candidate and shows to be a promising alternative for ITO containing the rare element indium.

7 Acknowledgement

First of all I would like to thank prof.dr. P.M. Koenraad for giving me the opportunity to do research in the splendid atmosphere the PSN (Photonics and Semiconductor Nanophysics) group has to offer. Furthermore I would like to thank dr. S. Kölling, A. Cavalli and M.Y. Swinkels for their guidance, support and valuable advice.

Secondly I would like to thank dr. V. Zardetto for the ALD of the samples and the clean room technicians drs. E. Smalbrugge and ing. T. de Vries for the training and aid in the clean room.

Finally I would like to thank everyone in the PSN group for the friendly atmosphere. Furthermore I would like to thank my girlfriend, parents and brother for the constant support.

8 Literature

References

[1] BP Group. Statistical review of world energy 2014. internet, Referenced to on 31/05/2015. http://www.bp.com/en/global/corporate/about-bp/energy-economics/statistical-review-of-world-energy.html.

[2] G. Counts A. Riddell, S. Ronson and K. Spenser. Towards sustainable energy: The current fossil fuel problem and the prospects of geothermal and nuclear power. internet, Referenced to on 31/05/2015. http://web.stanford.edu/class/e297c/trade_environment/energy/hfossil.html.

[3] C. Philibert. The present and future use of solar thermal energy as a primary source of energy. *IEA*, 2005.

[4] Z. Shanan. 13 charts on solar panel and growth trends. internet, Referenced to on 31/05/2015. http://cleantechnica.com/2014/09/04/solar-panel-cost-trends-10-charts/.

[5] Jesper Wallentin et al. Inp nanowire array solar cells achieving 13.8% efficiency by exceeding the ray optics limit. *Sciencemag*, 339:1057, 2013.

[6] C. Honsberg and S. Bowden. Surface recombination. internet, Referenced to on 15/05/2015. http://www.pveducation.org/pvcdrom/design/surface-recombination.

[7] Y. Cui E. Garnett, M. Brongersma and M. McGehee. Nanowire solar cells. *The Annual Review of Materials Research*, 2011.

[8] D. Orenstein. Light-absorbing nanowires may make better solar panels. internet, Referenced to on 15/05/2015. http://news.stanford.edu/news/2009/july8/light-absorbing-nanowires-070609.html.

[9] M. E. et al. Reimer. Bright single-photon sources in bottom-up tailored nanowires. *Nat. Commun. 3:737 doi: 10.1038/1746*, 2012.

[10] S. Sze and K. Ng. *Physics of semiconductor devices*. Jhon Wiley and Sons Inc., 3 edition.

[11] Y. Cui et al. Efficiency enhancement of inp nanowire solar cells by surface cleaning. *Nano Letters*, 13(9):4113 till 4117, 2013.

[12] J. Joyce et al. Efficiency enhancement of ultralow surface recombination velocity in inp nanowires probed by terahertz spectroscopy. *Nano Letters*, 12(10):4325 till 5330, 2012.

[13] R. LaPierre. Iii -v nanowire solar cells. Communications and Photonics Conference and Exhibition, 2011, Referenced to on 19/06/2015.

[14] V. Dubrovskii. *Nucleation Theory and Growth of Nanostructures*. Springer.

[15] D. Meier and D. Schroder. Contact resistance: Its measurement and relative importance to power loss in a solar cell. *IEEE transactions on electron devices*, 31(5):647 till 653, 1984.

[16] A. Pierret et al. Generic nano-imprint process for fabrication of nanowire arrays. *Nanotechnology*, 21, 2010.

[17] M.. Borgstrom et al. In situ etching for total control over axial and radial nanowire growth. *Nano Res*, 3:264 till 270, 2010.

[18] D. Schroder. *Semiconductor Material and Device Characterization*. Wiley-IEEE Press, 3 edition.

[19] Masato Yamashita and Mashiro Agu. Geometrical correction factor for semiconductor resistivity measurements by four-point probe method. *Japanese Journal of Applied Physics*, 23(11):1501, 1984.

[20] G. Tuttle. Contact resistance and tlm measurements. internet, Referenced to on 2/05/2015. `http://tuttle.merc.iastate.edu/ee432/topics/metals/tlm_measurements.pdfl`.

[21] Arthur H. Reading et al. High efficiency white leds with single-crystal zno current spreading layers deposited by aqueous solution epitaxy. *Optical Society of America*, 2011.

[22] Gabriele Fisichella et al. Micro- and nanoscale electrical characterization of large-area graphene transferred to functional substrates. *SciencemagThematic Series High-resolution electrical and chemical characterization of nm-scale organic and inorganic devices*, page 234 till 242, 2013.

[23] PMP research group. Advanced ald technologies. internet, Referenced to on 4/05/2015. `http://www.tue.nl/universiteit/faculteiten/technische-natuurkunde/onderzoek/onderzoekscluster-plasmas-en-straling/plasma-and-materials-processing-pmp/research/research-areas/advanced-ald-technologies/l`.

[24] H. Moshe and Y. Mastai. *Atomic Layer Deposition on Self-Assembled-Monolayers*. Materials Science - Advanced Topics.

[25] J.N. Hilfiker and R.A. Synowicki. Spectroscopic ellipsometry methods for thin absorbing coatings. *Society of Vacuum Coaters*, 2008.

[26] NanoPhysics. Sem edx. internet, Referenced to on 14/06/2015. `http://www.nanophysics.nl/Services/semedx.htmll`.

[27] F. Lacy. Developing a theoretical relationship between electrical resistivity, temperature, and film thickness for conductors. *Nanoscale Research Letters*, 6(1), 2011.

[28] S. Ishibashi et al. Low resistivity indium tin oxide transparant conductive films, effect of sputtering voltage on electrical property of films. *J. Vac. Sci. Technol.*, 1990.

[29] M. Farhan et al. Electrical and optical properties of indium tin oxide (ito) films by ion-assisted deposition (iad) at room temperature. *International Journal of Precision Engineering and Manufacturing*, 14(8):1465 till 1469, 2011.

9 Appendix

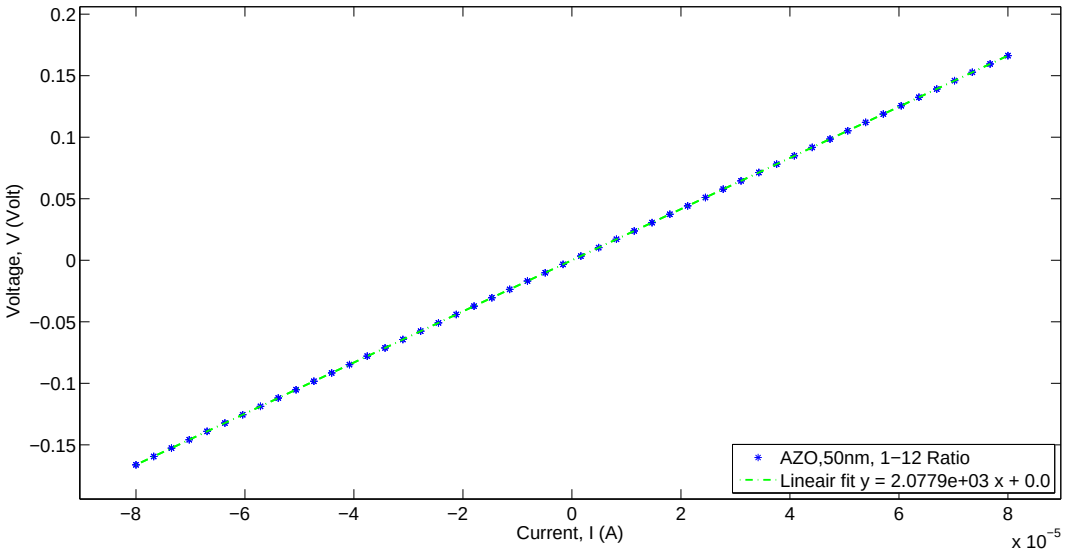

Figure 36: I-V characteristic for AlZnO (1:12) with a thickness of 50nm.

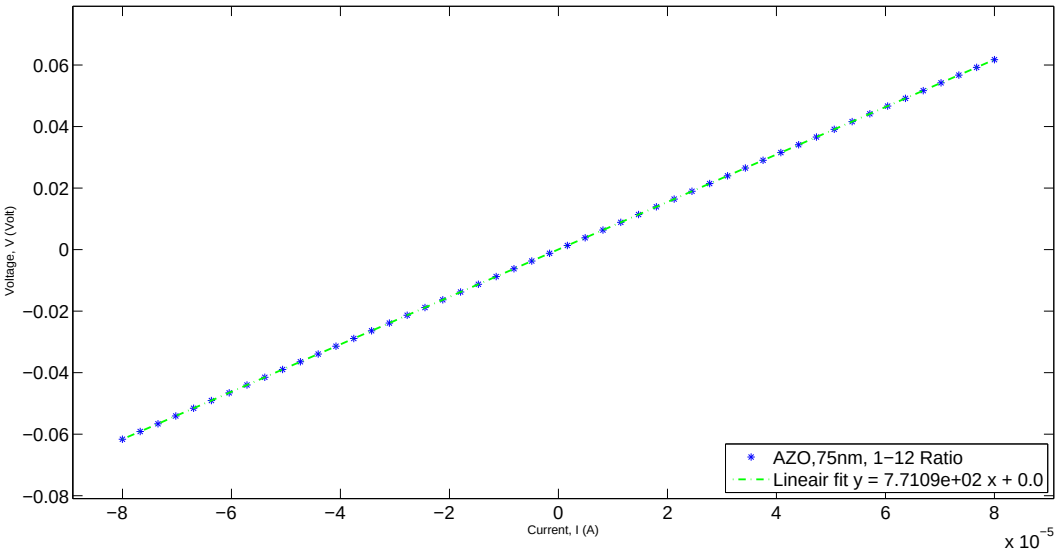

Figure 37: I-V characteristic for AlZnO (1:12) with a thickness of 75nm.

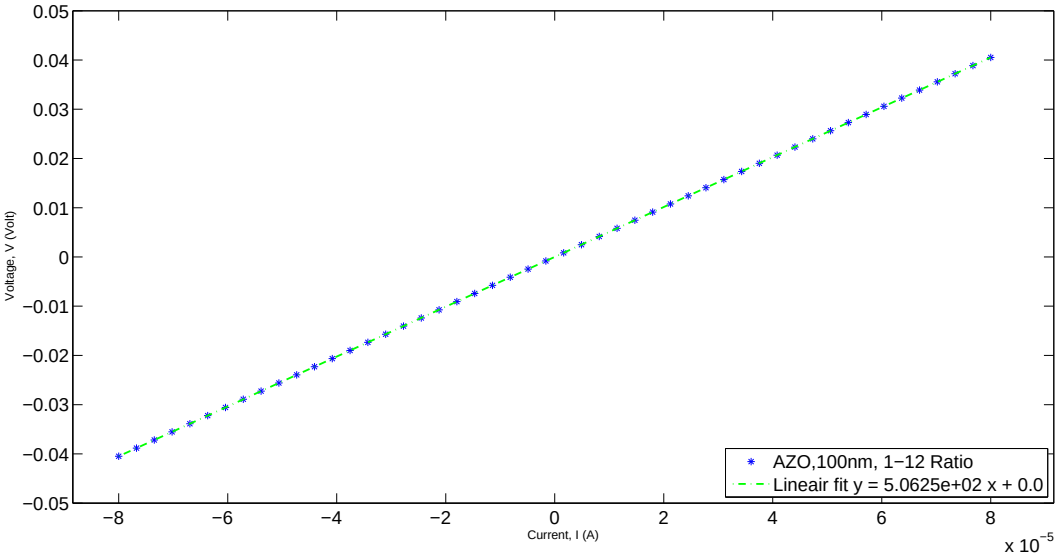

Figure 38: I-V characteristic for AlZnO (1:12) with a thickness of 100nm.

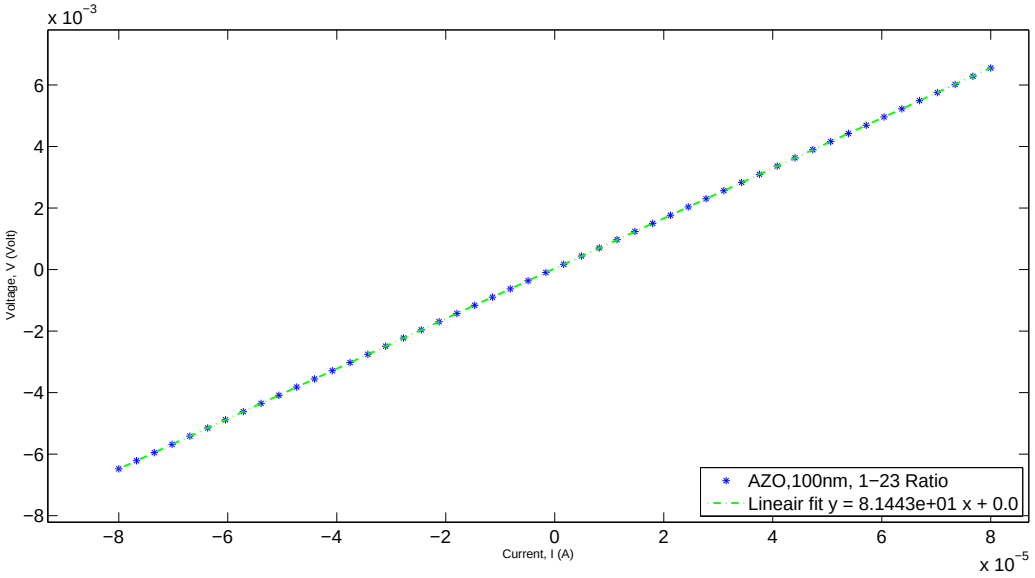

Figure 39: I-V characteristic for AlZnO (1:23) with a thickness of 100nm.

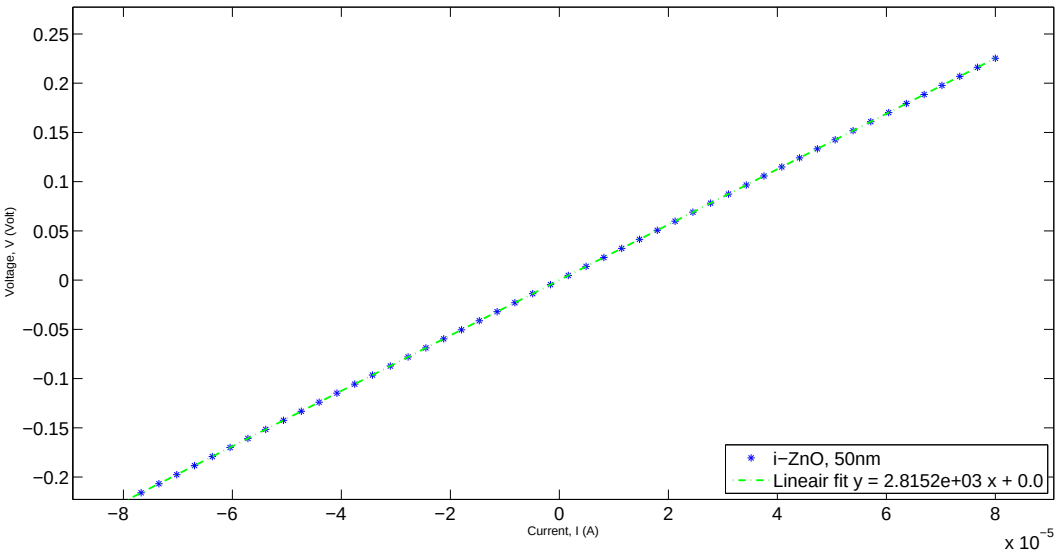

Figure 40: I-V characteristic for intrinsic ZnO with a thickness of 50nm.

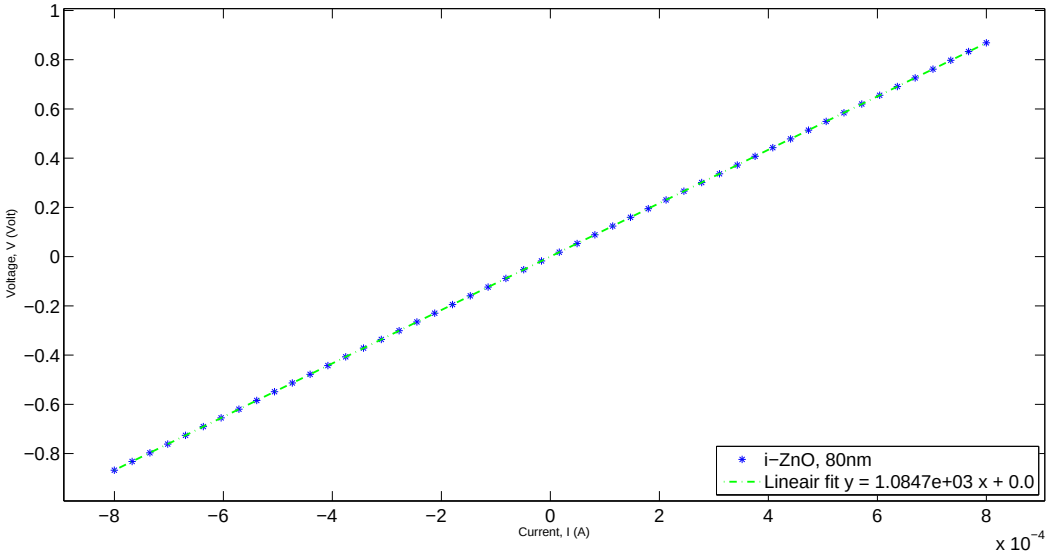

Figure 41: I-V characteristic for intrinsic ZnO with a thickness of 75nm.

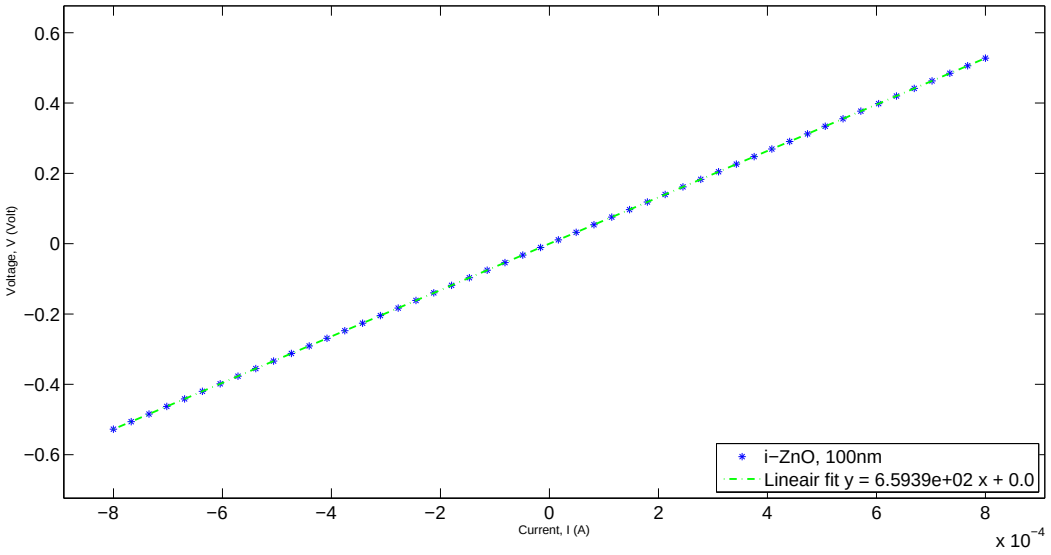

Figure 42: I-V characteristic for intrinsic ZnO with a thickness of 100nm.

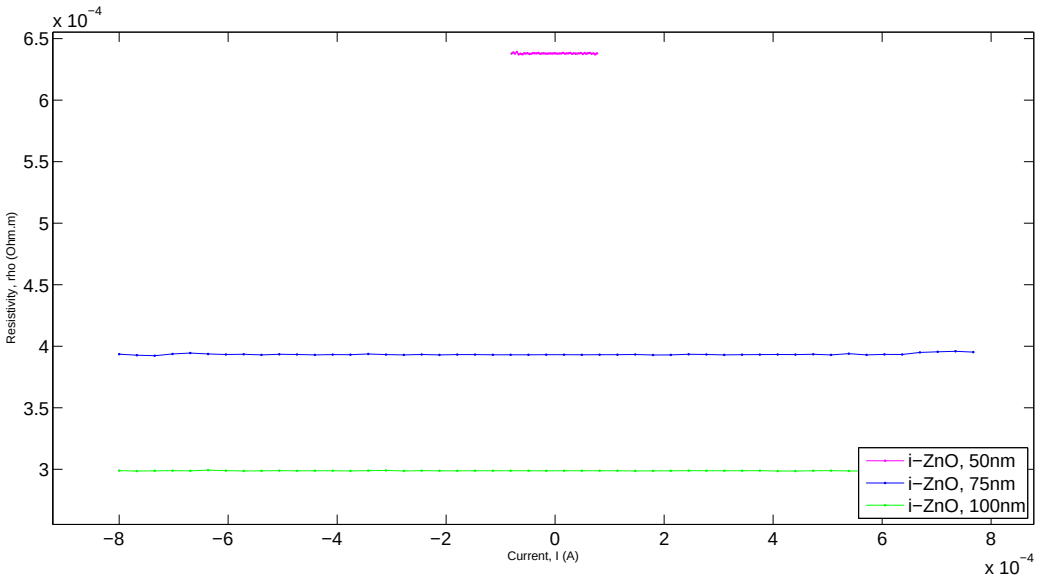

Figure 43: Resistivity versus current for intrinsic ZnO.

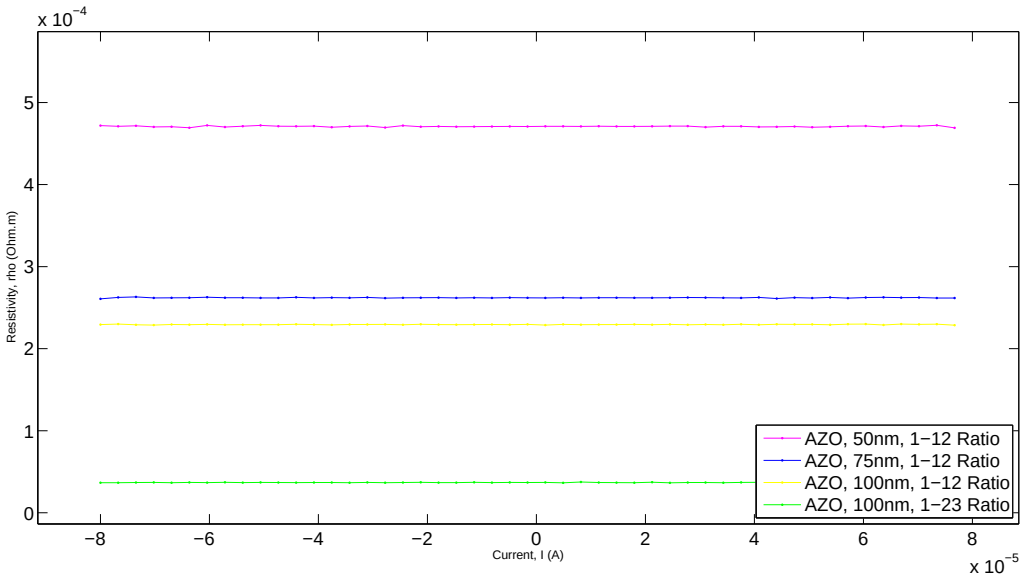

Figure 44: Resistivity versus current for AlZnO.

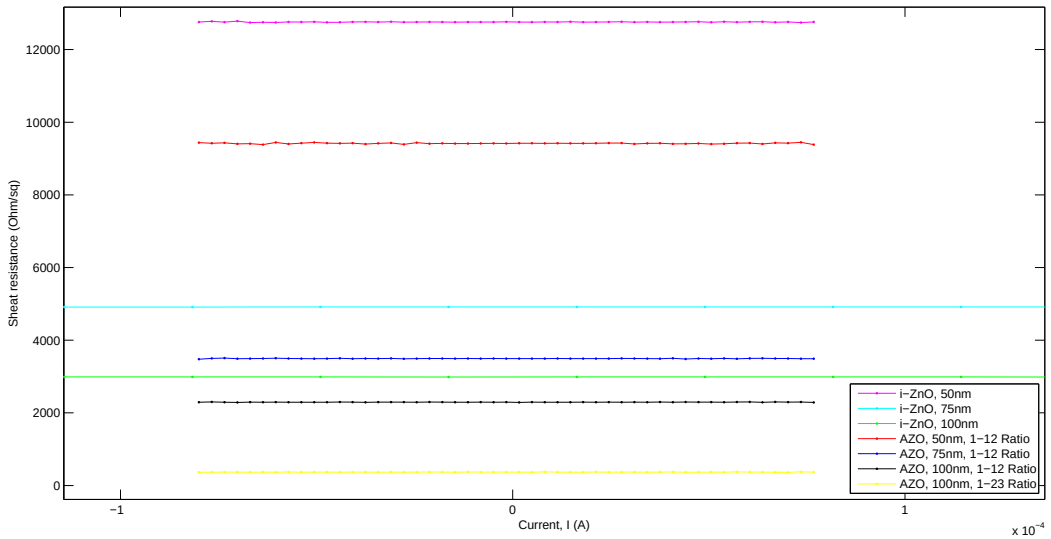

Figure 45: Sheet resistance versus current for all oxides.

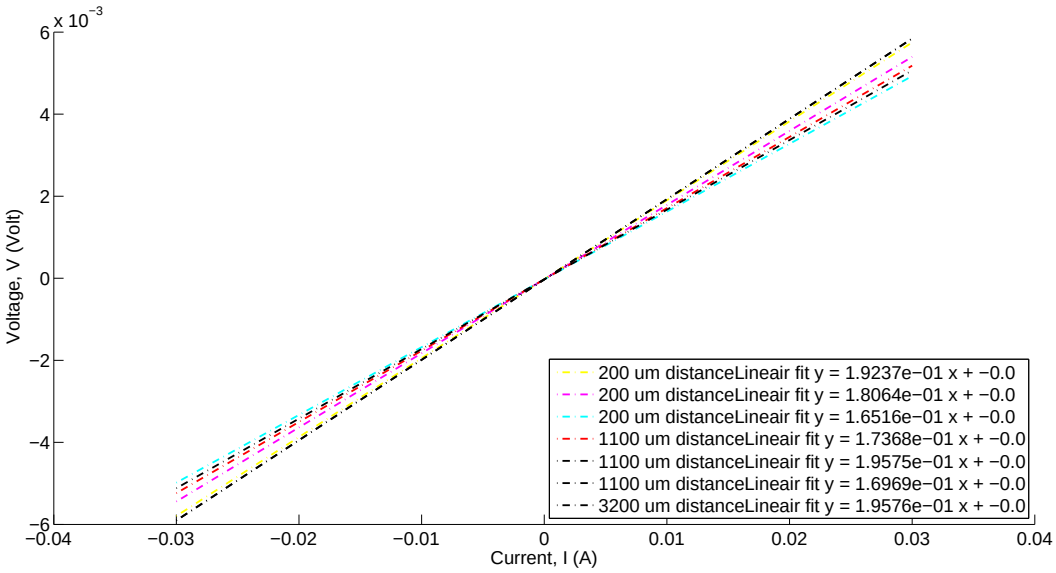

Figure 46: Raw data of the InP TLM measurement.